JfM PAPERS

Turbulent flow over isolated forested hills of varying shape and steepness

Edward G. Patton[1,*] ⓘ, John J. Finnigan[2,3] ⓘ, Ian N. Harman[2] ⓘ and Peter P. Sullivan[1] ⓘ

[1]NSF National Center for Atmospheric Research, Boulder, CO, USA

[2]Commonwealth Scientific and Industrial Research Organisation, Canberra, ACT, Australia

[3]Australian National University, Canberra, ACT, Australia

Corresponding author: Edward G. Patton; Email: patton@ucar.edu

To advance understanding of the influence hill-slope and hill-shape have on neutrally stratified turbulent air flow over isolated forested hills, we interrogate four turbulence-resolving simulations. A spectrally friendly fringe technique enables the use of periodic boundary conditions to simulate flow over isolated two-dimensional (2D) and three-dimensional (3D) hills of cosine shape. The simulations target recently conducted wind tunnel (WT) experiments that are configured to fall outside the regimes for which current theory applies. Simulation skill for flow over isolated 3D hills is demonstrated through matching the canopy and hill configuration with the recently conducted WT experiments and comparing results. The response of the mean and turbulent flow components to 2D versus 3D hills along the hill-centreline are discussed. The phase and amplitude of spatially varying flow perturbations over forested hills are evaluated for flows outside the regime valid for current theory. Flow over isolated 2D forested hills produces larger amplitude vertical motions on a hill's windward and leeward faces and the speed-up of the mean wind compared with that over isolated 3D forested hills at the hill-centreline. The 3D hills generate surface pressure minima over hill-crests that are only half the magnitude of those over 2D hills. The spatial region over which hill-induced negative pressure drag acts increases with increasing hill steepness. Assumptions in partitioning the flow into an upper layer with an inviscid response to the hill's pressure field are robust and lead to solid predictions of hill-induced perturbations to the mean flow; however, applying those assumptions to predict the evolution of the turbulent moments only provides approximate explanations at best.

Key words: turbulent boundary layers, topographic effects, turbulence theory

E.G. Patton, J.J. Finnigan, I.N. Harman and P.P. Sullivan

1. Introduction

Over 20 % of the Earth's surface can be characterized as hilly or mountainous terrain (e.g. Körner *et al.* 2005). Although tall mountainous regions of the world garner substantial focus in meteorology (e.g. Bougeault *et al.* 2001; Grubišić *et al.* 2008; Houze *et al.* 2017), the Earth's hypsographic curve interestingly shows that most of Earth's terrain is less than 1000 m in height (e.g. Lagrula 1968; Cawood *et al.* 2022). Even in large-scale mountainous terrain, terrain height spectra demonstrate substantial variance at small scales (e.g. Young & Pielke 1983). While today's weather, air pollution and climate models can potentially resolve the larger-scale terrain features (e.g. mountains), the ability to resolve gentle small-scale hills currently remains beyond reach in larger-scale models. Due to the prevalence of small-scale hills, understanding their influence on turbulent flow is also essential for proper measurement interpretation, and for describing pollutant, aerosol and seed transport, and for predicting wind throw and wind energy availability (e.g. Finnigan *et al.* 2020).

Under neutrally stratified conditions, inviscid incompressible flow over a low symmetric obstacle produces a pressure minima occurring at the obstacle crest but does not generate any resistance (drag) because the pressure perturbation remains symmetric relative to the obstacle in the absence of any momentum stress (e.g. d'Alembert 1752; Calero 2018). In laminar incompressible flow, the addition of finite viscosity ensures a thickening of the boundary layer (a greater separation of the streamlines) in a hill-like obstacle's lee due to the spatially varying action of viscous drag which produces a pressure perturbation phase-shifted slightly downstream relative to the obstacle resulting in form drag (typically referred to as sheltering, e.g. Prandtl (1904)). Turbulent incompressible flows over hills also produce form drag through sheltering but the turbulent stresses dominate the smaller viscous stresses resulting in even larger pressure asymmetry relative to the hill shape producing even larger drag (e.g. Jackson & Hunt 1975; Britter, Hunt & Richards 1981; Hunt, Leibovich & Richards 1988; Belcher, Newley & Hunt 1993). Characteristics of the hill can alter the flow's evolution over the obstacle, e.g. flow over steeper hills induces larger amplitude pressure perturbations and this obstacle-induced pressure perturbation can generate a sufficiently large near-surface adverse pressure-gradient on the hill's lee that downward turbulent transport of momentum from aloft becomes insufficient to counter the adverse pressure-gradient producing flow separation; whether the flow separates or not dramatically alters the pressure field and hence the overall form drag felt by the outer flow (e.g. Taylor, Mason & Bradley 1987; Finnigan *et al.* 1990; Wood & Mason 1993; Athanassiadou & Castro 2001). Because surface roughness alters the turbulence, variations in surface roughness also modulate flow responses to hills and the induced separation (e.g. Britter *et al.* 1981; Ayotte & Hughes 2004; Tamura, Okuno & Sugio 2007). Flow over two-dimensional (2D) versus three-dimensional (3D) hills (e.g. ridges versus isolated hills) also differs substantially because of the ability for flow over 3D hills to divert around the hill, which produces spanwise shear around the edges of and in the lee of the hill altering the turbulence and separation by generating additional instabilities and vortices (e.g. Mason & Sykes 1979; Hunt & Snyder 1980; Mason & King 1985; Arya & Gadiyaram 1986; Gong & Ibbetson 1989; Ishihara, Hibi & Oikawa 1999; Liu *et al.* 2019*a*,*b*, 2020).

Because mountainous and hilly terrain compresses climate zones and creates small-scale habitat diversity, these regions support more than one quarter of the Earth's terrestrial biodiversity (e.g. Körner *et al.* 2005). Hilly terrain is therefore frequently forested. Finnigan & Belcher (2004) demonstrated using linearized theory that because forests interact with the flow through pressure drag, forests on hills can shift the

hill-induced pressure perturbation enough to induce separation at notably smaller slopes than expected over hills of similarly specified roughness. Finnigan & Belcher's (2004) theory also predicts that flow separation should depend on the distribution and density of the canopy elements, which Patton & Katul (2009) later confirmed. Researchers such as Wilson, Finnigan & Raupach (1998), Poggi *et al.* (2007) and Ross (2008) discussed that within-canopy turbulence mixing length scales vary with position over sinusoidally repeating forested hills. When investigating turbulent flow over observed Amazonian terrain, Chen, Chamecki & Katul (2020) found separated flow even in the lee of small bumps, and Chamecki *et al.* (2020) and Chen & Chamecki (2023) showed that imbalances in above-canopy turbulent kinetic energy (TKE) budgets can result from upstream terrain influences. With the exception of Chamecki *et al.* (2020), Chen *et al.* (2020) and Chen & Chamecki (2023), much of this literature discussing turbulence over forested hills has focused on 2D sinusoidally repeating hills.

To our knowledge, Finnigan & Brunet (1995) represents the first effort describing within- and above-canopy turbulent flow over isolated forested hills, where they documented that above-canopy streamlines dip into the canopy at approximately one-third the way up the windward side of a 2D isolated hill that can eliminate (or even reverse) the inflection point in the mean velocity profile expected in canopy-flows (e.g. Raupach, Finnigan & Brunet 1996; Finnigan, Shaw & Patton 2009); a phenomenon that has important implications for turbulence production at canopy-top. Neff & Meroney (1998) found that canopy-gaps influence hill-induced fractional speed-up factors and flow separation. Through two-point correlation analysis, Dupont & Brunet (2008) noted that turbulence in the intermittent leeward separation zone is not correlated with canopy-top turbulence on the windward side of the hill. Grant *et al.* (2015) found key features predicted by Finnigan & Belcher's (2004) theory in their field measurements over an isolated forested ridge. For a given hill shape, Ma *et al.* (2020) demonstrated that variation in a canopy's morphology modulates the position, strength and depth of the leeward separation bubble. Similar to Wood (2000) who discussed flow over hills with unresolved roughness, Tolladay & Chemel (2021) demonstrated resolution influences on key turbulence statistics in large-eddy simulation (LES) of flow over the same isolated forested ridge as that studied by Ma *et al.* (2020). These efforts have enhanced the general understanding of the role tall vegetation plays in modulating turbulent flow over infinitely long isolated ridges; how canopies modulate turbulence over 3D hills remains understudied.

Towards understanding the role that hill shape and slope play in modulating turbulence, we analyse four LESs of turbulent flow over isolated forested hills. These four simulations include two each at two different hill slopes. For each hill slope, the simulations conducted include one targeting flow over an infinitely wide 2D hill and one over an axisymmetric 3D hill. In collaboration with the effort reported here, colleagues conducted a comprehensive WT experiment studying neutrally stratified turbulent over 3D forested hills (figure 1, Harman & Finnigan 2018). The numerical simulations attempt to reproduce the physical WT simulations over axisymmetric 3D hills (Harman & Finnigan 2018) and 2D hills.

The outline of this manuscript is as follows: § 2 discusses current theory describing turbulent flow over forested hills. Section 3 describes the simulations investigated. Section 4 outlines the techniques used to analyse the simulation data. Section 5 compares the simulation results against WT measurements from Harman & Finnigan (2018). Section 6 describes the mean flow and turbulence response to variations in hill shape and slope. Section 7 interrogates turbulence/mean-flow phase relationships at key heights above the surface towards advancing current theory, and § 8 summarizes the findings.
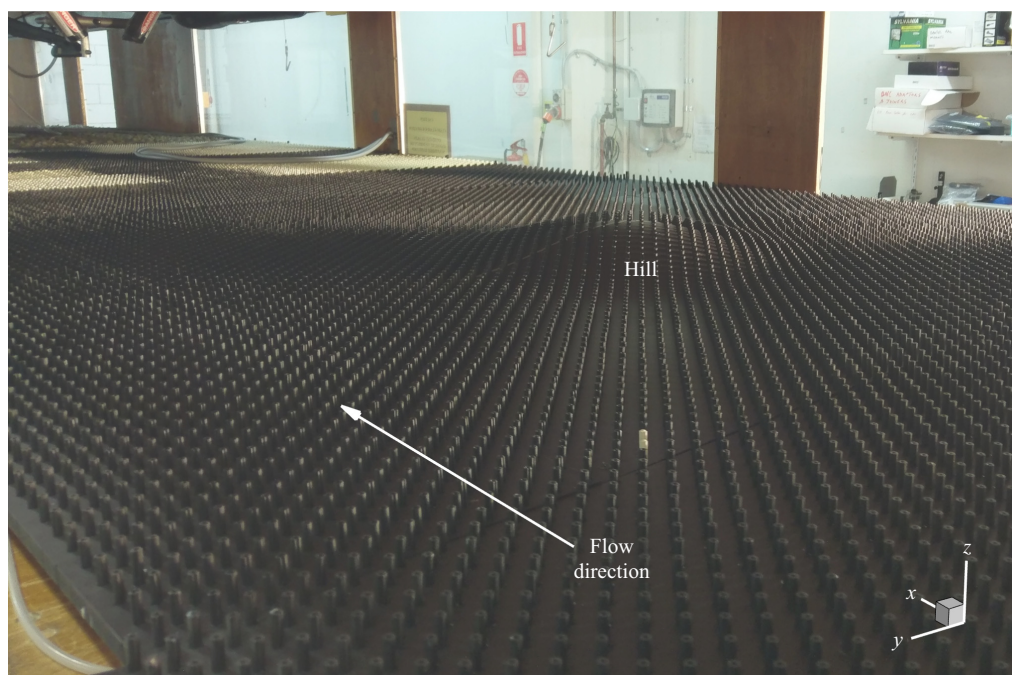
Figure 1. A photograph of the forested isolated axisymmetric 3D steep ($s_m = 0.26$) cosine hill surface in the wind tunnel (WT) (Harman & Finnigan 2018).

2. Current theory describing turbulent flow over forested hills

Current analytic theory of turbulent shear flow over low hills (e.g. Jackson & Hunt 1975; Hunt *et al.* 1988; Belcher *et al.* 1993) has provided an enduring and consistent framework for analysis and understanding of flow over low hills and even over steeper hills upwind of the separation region. The theory divides the flow into different layers, where the perturbations to the mean flow caused by the hill are governed by distinctly different dynamics. Separate solutions to the flow equations are found for each layer and then these are matched asymptotically between the layers. For hills of sufficiently low-slope to ignore flow separation, Hunt *et al.* (1988) defined two main regions: (i) the outer region, where the response to the pressure field generated by flow over the hill is inviscid, and (ii) the inner region, where perturbations to the turbulent Reynolds stresses affect the perturbations to the mean flow. Each of these regions was further divided into two layers. The middle layer, of depth h_m, is the lower part of the outer region through which flow responses are inviscid but rotational to accommodate shear in the approach flow. In the upper layer, extending from h_m to the top of the boundary layer, flow responses are irrotational and can be computed by potential theory. The inner region consists of the shear stress layer of depth h_i, and the thin inner surface layer, of depth l_s, which allows formal matching with a surface boundary condition.

Finnigan & Belcher (2004) extended the analytic theory of Hunt *et al.* (1988) to hills covered by tall plant canopies by replacing the thin inner surface layer by a deep plant canopy parameterized by linearized flow equations in the upper canopy but where the unavoidably nonlinear dynamics in the lower canopy were treated heuristically. Harman & Finnigan (2009, 2013) further developed Finnigan & Belcher (2004) to accommodate more realistic 2D hills, and then Harman & Finnigan (2021) extended the theory to 3D hills.

In all of these small perturbation theories, whether over hills covered by a rough surface or a tall canopy, identifying the depths of the inner shear stress layer, h_i, and the middle layer, h_m, is critical to applying the theory. To derive the formula for h_m, Hunt *et al.* (1988) assumed that the flow approaching the hill could be described by a logarithmic profile in equilibrium with the upstream surface while in the inner shear stress layer h_i, the interdependence of the perturbations to the turbulent shear stresses and the perturbations to the mean shear are assumed to obey the same mixing length flux-gradient relationship as in an equilibrium log law. Finnigan & Belcher (2004) relies on the same formulae for h_m and h_i as Hunt *et al.* (1988).

The formulae for h_m and h_i assume the flow over the hill remains attached (i.e. no flow separation). Over steeper 2D hills and over 3D hills, this assumption breaks down. If the flow separates, streamlines that were following the surface contour upwind leave the surface and delineate the boundary of a separation bubble. Downwind of the separation point the scale of the largest turbulent eddies increases abruptly. In the attached flow the largest eddies are limited by the local distance to the surface but after separation the largest eddies span the bubble depth, which is typically $O(H)$ with H representing the hill height. While the streamlines approaching a 3D hill in its plane of lateral symmetry go over the hill-centreline, streamlines to either side are deflected forming space curves whose principal normals intersect the hill surface at right angles (Finnigan 2024).

As fluid parcels above the canopy advect over the hill, changes to the Reynolds stresses reflect the competing effects of two processes. First, the existing eddies are stretched and rotated by the mean flow as they follow the mean streamlines. Second, nonlinear interactions between the eddies will tend to equalize *TKE* between their orthogonal components u', v' and w', and to transfer TKE to finer scale eddies where it is ultimately dissipated to heat through the action of viscosity. These effects are represented formally in the conservation equations for the turbulent normal and shear stresses, $\langle u'^2 \rangle$, $\langle v'^2 \rangle$, $\langle w'^2 \rangle$, $\langle u'w' \rangle$, $\langle v'w' \rangle$ and *TKE*, where $TKE = (\langle u'^2 \rangle + \langle v'^2 \rangle + \langle w'^2 \rangle)/2$. In these equations, the so-called production terms describe the transfer of kinetic energy from the mean flow to the larger energy-containing eddies of the turbulence while the turbulent diffusion and pressure-strain terms describe the nonlinear interactions between these eddies, which break them down and destroy their coherence. These nonlinear interactions determine τ, the time over which the large eddies remain coherent enough to receive energy directly from the mean flow. Here τ can be taken as $\tau \sim TKE/\epsilon$, where ϵ is the rate of viscous dissipation of TKE. This definition is strictly only applicable to equilibrium situations, where the rate of viscous dissipation is in balance with the transfer of kinetic energy from the mean flow to the turbulence, but we will assume that is also indicative of the rate at which these large eddies lose their coherence as they interact with each other during their passage over the hill.

In regions where the time scale of hill-induced changes in the mean flow is small compared with τ (i.e. in the so-called rapid distortion regimes), the turbulent stresses will reflect their recent history of straining and rotation by the mean flow and Hunt *et al.* (1988) assumes that this will be the case in the outer region in general and in the middle layer in particular. In regions where mean flow changes are slow compared with τ, the turbulence will approach a state of local equilibrium between the rate of straining by the mean flow and the resulting Reynolds stresses so that their relationship can be described by an eddy viscosity. Current theory assumes that we should observe this behaviour in the inner shear stress layer, $z < h_i$.

Beneath the inner layer and above the ground surface lies the canopy layer, which introduces additional length scales (L_c and h_c), through the addition of canopy drag and the no-slip condition at the surface. In the canopy, turbulent stresses are complicated by wake

production, W_p, i.e. the production of turbulent eddies at scales defined by the canopy elements and associated short-circuiting of the inertial energy cascade (Finnigan 2000; Shaw & Patton 2003). In addition, viscous dissipation increases by the work performed by the turbulence against the viscous drag of the canopy elements (Ayotte, Finnigan & Raupach 1999; Shaw & Patton 2003). For dense canopies ($h_c/L_c > 1$), canopy drag eliminates the importance for the flow dynamics of shear stress at the underlying surface but at the same time ensures strong vertical gradients in turbulent stresses. Finally, behind the hill crest, the strong adverse pressure gradient can cause reversed flow and separation, which introduces the hill height H as an additional length scale affecting the turbulence.

3. Simulation description and configuration

Numerical models of turbulent flow over forested hills take many forms that each provide value with varying levels of accuracy and cost (see recent review by Finnigan *et al.* (2020)). Analytical models provide extremely timely solutions, but typically linearize the nonlinear equations that describe turbulent flow (e.g. Finnigan & Belcher 2004; Poggi *et al.* 2008; Harman & Finnigan 2009, 2013). Reynolds-averaged Navier–Stokes models solve the full nonlinear equations but averaged over space and time such that the influence of turbulence is fully parameterized (e.g. Wilson *et al.* 1998; Katul & Chang 1999; Ross & Vosper 2005, among others). Similar to Reynolds-averaged Navier–Stokes, LES also solves the full nonlinear equations but relies on relatively isotropic grids and only spatially averages (or filters) the equations at scales smaller than the grid resolution, such that the largest scales of turbulence (i.e. those performing most of the transport) are resolved by the grid and only the smallest scales of turbulence (which primarily act to dissipate energy) must be parameterized (e.g. Moeng & Sullivan 2015). Although it is computationally expensive, LES has become a close counterpart to field and laboratory experiments over the past 30 plus years because of its ability to accurately simulate the time-evolving and spatially evolving response of turbulence to varying forcing over complex surfaces (e.g. Wood 2000; Patton & Katul 2009; Sullivan, McWilliams & Patton 2014; Chamecki *et al.* 2020).

In our LES, the governing equations describe 3D time-dependent turbulent winds in a dry incompressible Boussinesq atmospheric boundary layer, including (i) three transport equations for momentum $\rho\boldsymbol{u}$, (ii) a transport equation for a conserved scalar variable, (iii) a discrete Poisson equation for a pressure variable p to enforce incompressibility and (iv) closure expressions for subgrid-scale (SGS) variables, e.g. an equation for SGS TKE e (see Sullivan *et al.* 2014). The physical processes included in the LES boundary-layer equations include, temporal time tendencies, advection, pressure gradients, divergence of SGS fluxes, buoyancy, resolved turbulence, and in the case of the SGS e equation also diffusion and dissipation.

Explicit spatial filtering of the momentum equations in the presence of vegetative-canopy elements generates terms representing canopy-induced pressure and viscous drag (Finnigan & Shaw 2008) which are parameterized using a time-dependent and local velocity-squared type drag law, e.g.

$$F_c = - c_d \, a \, |\boldsymbol{u}| \, \boldsymbol{u}, \tag{3.1}$$

where, a is the canopy's frontal area density and c_d is a drag coefficient describing the canopy's efficiency at absorbing momentum. Dissipation in the SGS energy equation is also augmented by the work SGS motions perform against the canopy-induced form drag. See Shaw & Patton (2003), Patton & Katul (2009) and Patton *et al.* (2016) for further details of the canopy representation in the LES.

By applying a transformation to the physical space coordinates (x, y, z) that maps them onto flat computational coordinates (ξ, η, ζ), Sullivan *et al.* (2014) adapted our flat LES (Sullivan & Patton 2011) to a situation with a 3D time-evolving lower boundary shape $h = h(x, y, t)$. The current simulations use this same framework, but impose a time-independent surface, e.g. $h = h(x, y)$ where the maximum hill slope $s_m = \max(\partial h / \partial x)$. Of importance is that we transform the coordinates, not the flow variables. Therefore, horizontal velocity components (u, v) are defined in a right-handed Cartesian coordinate system parallel to the flat surface surrounding each hill (with u aligned with the imposed pressure gradient force in the $+x$ direction, and v positive to the left of the imposed pressure gradient force in the $+y$ direction), and vertical velocity (w) is defined positive upward from the underlying flat surface (the $+z$ direction) aligned opposite to the gravitational force (although the flow under consideration is neutrally stratified, so gravitational forces are ignored).

The simulations discretize a $4096 \times 2048 \times 512$ m^3 domain using $2048 \times 1024 \times 256$ grid points. The computational mesh in physical space is surface following and non-orthogonal. Vertical grid lines are held fixed at a particular (x, y) location but the horizontal grid lines undergo vertical translation according to the vertical variation of the underlying surface. While the grid resolution in the horizontal directions is fixed for all horizontal locations, the vertical grid is refined near the surface to resolve near-surface/canopy processes and is then algebraically stretched above the canopy to push the upper boundary far above the hill to minimize any influence of the upper boundary on the hill-induced pressure field. Care is taken to ensure that every grid volume uses an aspect ratio no larger than $5 : 1$ attempting to reasonably satisfy isotropy assumptions used to close the equations in the SGS model.

Spatial differencing is pseudospectral in the horizontal computational directions (ξ, η) and is second-order finite difference in ζ. Time stepping uses a low-storage third-order Runge–Kutta scheme, and the time step δt is picked dynamically based on a fixed Courant–Fredrichs–Lewy number.

An important development for this effort involves implementing a turbulent inflow fringe (or precursor) method which is compatible with our pseudospectral spatial differencing and third-order Runge–Kutta time differencing (Schlatter, Adams & Kleiser 2005; Munters, Meneveau & Meyers 2016) to enable simulation of flow over isolated 2D and 3D hills. The strategy involves simulating two interconnected periodic domains, where the flow in the upwind domain is periodic and representative of flow over an infinitely long horizontally homogeneous forested surface. The outflow of that upwind domain serves as inflow for the downwind domain containing the hill. In the second domain at the boundary far downstream from the hill, nudging terms are applied over the downwind-most 102 grid points (from grid points 1946–2048) to force the exit flow of the larger downwind domain to match the flow exiting the upstream region (note that 102 grid points is 20 % of the upwind domain). Hence both domains use periodic boundary conditions in the x direction, but the flow impinging on the hill is unaware of any upstream hills. It is important to note two things: (i) the size of the upstream inflow domain dictates the largest scales of motion impinging on the hill located in the downstream domain, and (ii) the chosen fringe strategy used in these simulations was developed prior to and differs from the two-domain strategy discussed in Sullivan *et al.* (2020, 2021) that ensures decoupling of inflow conditions from any slight imperfections in the spectral tapering (e.g. Inoue, Matheou & Teixeira 2014) and which enables inclusion of Coriolis and buoyancy forces. (For these reasons, we recommend using the technique described by Sullivan *et al.* (2020, 2021) for future studies.) Figure 2 shows the total extent of the horizontal domain for the two steeper hill configurations ($s_m = 0.26$). The blue lines in figure 2 mark the boundaries
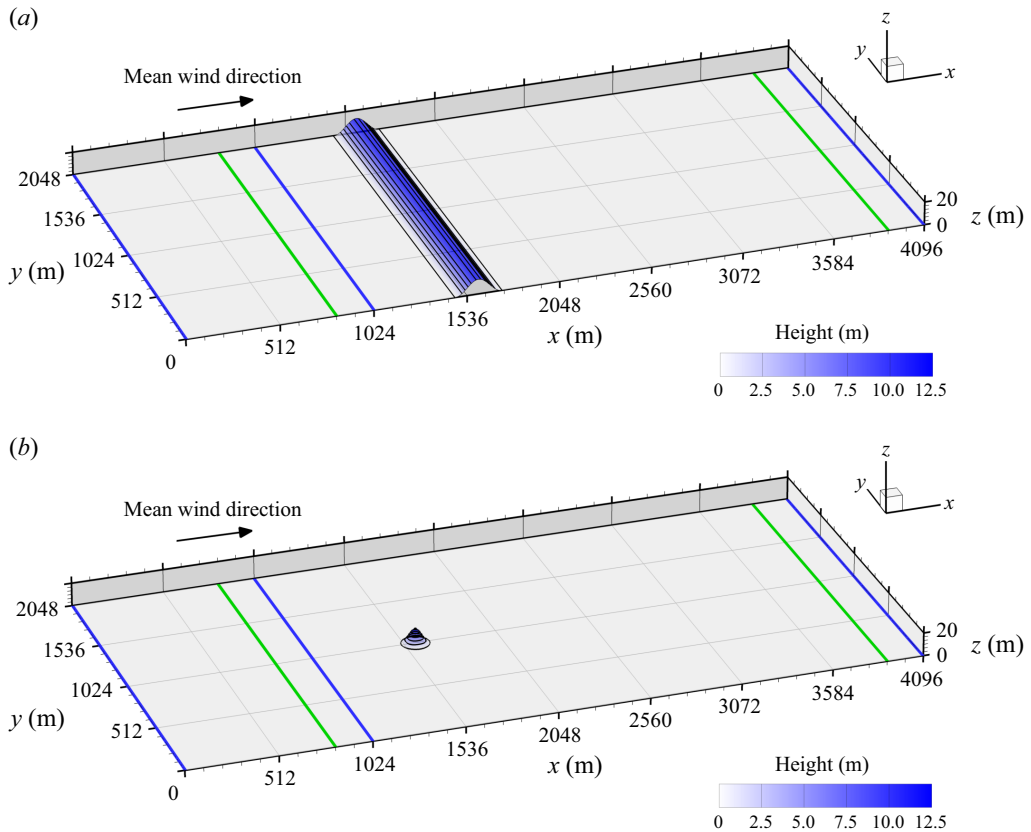
Figure 2. Example of the horizontal domains used and the idealized cosine-shaped 2D and 3D hills. Panel (*b*) reflects the axisymmetric case with $L = L_y = L_x$. The blue line spanning the domain at $x = 1024$ m depicts the downwind boundary of the horizontally homogeneous periodic region, while the green line spanning the domain at $x \sim 3892$ m depicts the beginning of the fringe region where the solutions begin to be nudged back to those at the downwind edge of the upwind periodic region starting at the green line located at $x \sim 820$ m. Periodic boundary conditions are imposed in the y-direction. The vertical domain extends up to 512 m.

where periodicity in the x direction is enforced. The green lines in figure 2 mark the starting point of the region where the nudging algorithm operates, with the left-hand side showing the horizontally homogeneous region used to nudge the downstream flow back to horizontally homogeneous flow that is unaware of the hill and the right-hand side showing the region that is nudged back to the upwind conditions. Periodic boundary conditions are imposed in the lateral (y) direction, the upper boundary is a frictionless rigid lid, and the lower boundary beneath the trees uses a rough-wall neutrally stratified drag law with a surface roughness length $z_\circ = 1 \times 10^{-3}$ m.

To minimize the computational expense, all the simulations are generated by first integrating a smaller $512 \times 512 \times 256$ grid point flat-domain simulation out in time using periodic horizontal boundary conditions until the initially laminar flow develops from divergence free random fluctuations into 3D turbulence that is in equilibrium with the imposed pressure gradient. Upon reaching equilibrium, a restart volume is saved. This volume is then mirrored one time in the lateral (y) and four times in the downwind (x) directions to create a fully turbulent initial condition for the full large-domain simulations. The code is then reconfigured to: (i) restart from this larger volume, and (ii) run using the precursor inflow boundary condition in the along-wind (x) direction. Upon restart, a

hill is gradually grown into the downwind portion of the domain over a period of 400 s. Averaging begins after integrating forward in this configuration for approximately one large-eddy turnover time to allow the turbulence to evolve into the new configuration. Running on 2048 CPUs on an HPE SGI ICE XA system (Computational and Information Systems Laboratory 2019), the (2D; 3D)-hill simulations required approximately (77; 366) wallclock hours, respectively.

As in the WT measurements (Harman & Finnigan 2018), the flow is neutrally stratified (no buoyancy) and Coriolis forces are ignored. The hills are of cosine shape,

$$h(x, y) = H \cos^2 \left(\frac{\pi \, \widehat{x}}{4} \right) \qquad \text{when} \quad |\widehat{x}| \leq 2, \tag{3.2}$$

$$h(x, y) = 0 \qquad \text{when} \quad |\widehat{x}| > 2, \tag{3.3}$$

where, H is the hill height. In the 2D-hill case,

$$\widehat{x} = \frac{x - x_\circ}{L_x}, \tag{3.4}$$

and, in the 3D-hill case,

$$\widehat{x} = \left[\left(\frac{x - x_\circ}{L_x} \right)^2 + \left(\frac{y - y_\circ}{L_y} \right)^2 \right]^{\frac{1}{2}}, \tag{3.5}$$

where L_x and L_y are the hill lengths at the hill half-height in the x and y directions, respectively, and $(x_\circ, y_\circ)$ represent the physical location of the hill crest. In the axisymmetric 3D hill simulations, $L_x = L_y = L$. Variations in hill steepness are generated by keeping H fixed and varying L. Scaling up the WT hills by a factor of 256, $H = 12.8$ m for all cases; see table 1 for the matching values of L. Figure 3 shows examples of the surfaces investigated with the LES. The x, y grid lines follow this surface and algebraically relax back to horizontal grid lines parallel to the upwind flat surface at approximately the domain half-height (see (4) in Sullivan *et al.* (2014), where we use $\varpi = 3$).

The canopy parameters are derived directly from measurements of the rods used in the WT experiments (Harman & Finnigan 2018). In the WT, the rods are 15 mm tall, 5 mm in diameter (d_r), and are spaced at 12.5 mm intervals in the x direction and 25 mm in the y direction. Hence, the number of rods per unit area $n_r = 3200 \, \text{m}^{-2}$ and the rods have a frontal area density $a = n_r \times r_d = 16 \, \text{m}^2 \, \text{m}^{-3}$ that is constant with height. Fitting the WT observed profiles with the rods installed on flat terrain (Harman & Finnigan 2018, figure 2a) to the Harman & Finnigan (2007) roughness sublayer (RSL) theory reveals that the rods have an effective canopy length scale $L_c = (c_d \, a)^{-1} = 110$ mm. Therefore, the drag coefficient c_d of the rods is 0.57. In the numerical simulations, these rod parameters are applied to a canopy of height $h_c = 3.84$ m resolved by nine grid points on the flat portion of the domain and by 10 grid points at the hill crest due to the terrain following co-ordinate system. To mimic the WT experiments, the canopy is prescribed to be horizontally homogeneous for all four simulations. Figure 1 shows an image of the WT configuration with the steep-sloped ($s_m = 0.26$) axisymmetric canopy-covered hill installed.

To classify the current simulations within the context of previous work, we first turn to the Hunt *et al.* (1988) and Finnigan & Belcher (2004) theories discussed in § 2. In both theories, the middle layer depth (h_m) is defined as $h_m \sim L \, [\ln(h_m/z_\circ)]^{1/2}$, and the inner layer depth (h_i) is defined as $h_i \sim 2 \, L \, \kappa^2 / \ln(h_i/z_\circ)$, where κ is von Kármán's constant. However, calculating h_i and h_m using these formulations can lead to physically implausible values over surfaces covered with tall roughness, i.e. h_i can end up being found at heights within the canopy of roughness elements (Finnigan *et al.* 1990). Therefore,

Case ID	Shape	s_m	L	u_*	F_p/u_*^2	F_c/u_*^2	F_τ/u_*^2	max $(\Delta u/u_b)_{h_c}$	max $(\Delta\sigma_u/\sigma_{u_b})_{h_c}$	max $(\Delta\sigma_w/\sigma_{w_b})_{h_c}$	max $(\Delta uw/uw_b)_{h_c}$
2D–0.16	2D	0.16	64.0	0.42	0.78	0.22	0.02	0.56 [−0.41]	0.11 [−0.34]	0.35 [0.88]	0.32 [−1.38]
3D–0.16	3D	0.16	64.0	0.40	0.46	0.20	0.12	0.42 [−0.34]	0.10 [−0.22]	0.26 [0.72]	0.75 [0.81]
2D–0.26	2D	0.26	38.4	0.42	2.69	0.22	0.01	0.80 [−0.31]	0.09 [−0.31]	0.37 [2.29]	0.68 [−1.30]
3D–0.26	3D	0.26	38.4	0.42	1.26	0.18	0.08	0.64 [−0.31]	0.19 [−0.16]	0.19 [1.30]	0.13 [1.09]

Table 1. Bulk parameters from each of the four simulations. Here s_m is the maximum hill slope ($\max(\partial h/\partial x)$), L is the length of the hill (m) in the streamwise direction x at half the hill height (so the total hill length is $4L$), u_* is the friction velocity (m s^{-1}) evaluated at $x = -4L$ and $z = h_c$ (consistent with u_* observed in the WT; when averaged over the entire upwind periodic domain, $u_* = 0.42$ m s^{-1} for all cases). Here $F_p = -\int_{-2L}^{2L} \langle p \rangle h_x \, dx$ is the streamwise surface pressure drag integrated over the hill (e.g. the hill-induced pressure force on the air) normalized by u_*^2, where $h_x = \partial h/\partial x$ is the x-varying hill slope), $F_c = -c_d \, a \int_{-2L}^{2L} \int_0^{h_c} \langle |u_i|u \rangle \, dz \, dx$ is the hill- and canopy-integrated drag induced by the canopy in the streamwise direction and $F_\tau = \int_{-2L}^{2L} \langle u'w' \rangle \, dx$ is the hill-integrated streamwise surface stress; the total drag felt by the flow over the hill $F_T = F_p + F_c + F_\tau$. Here $\max(\Delta u/u_b)_{h_c}$, $\max(\Delta\sigma_u/\sigma_{u_b})_{h_c}$, $\max(\Delta\sigma_w/\sigma_{w_b})_{h_c}$ and $\max(\Delta uw/uw_b)_{h_c}$ are the maximum hill- and canopy-induced speedup, standard deviation of streamwise and vertical velocity, and vertical flux of streamwise momentum increase at canopy top along hill centreline, respectively, where $\Delta u/u_b = [(\langle u \rangle - \langle u \rangle_b)/\langle u \rangle_b]$, $\Delta\sigma_u/\sigma_{u_b} = [(\sigma_u - \sigma_{u_b})/\sigma_{u_b}]$, $\Delta\sigma_w/\sigma_{w_b} = [(\sigma_w - \sigma_{w_b})/\sigma_{w_b}]$ and $\Delta uw/uw_b = [(\langle u'w' \rangle - \langle u'w' \rangle_b)/\langle u'w' \rangle_b]$ evaluated at a height of h_c above the local surface h, the notation $_b$ refers to a reference value upwind of the hill (Appendix A) and the adjacent values in square brackets reflects the x/L location where the maximum canopy-top value is found.
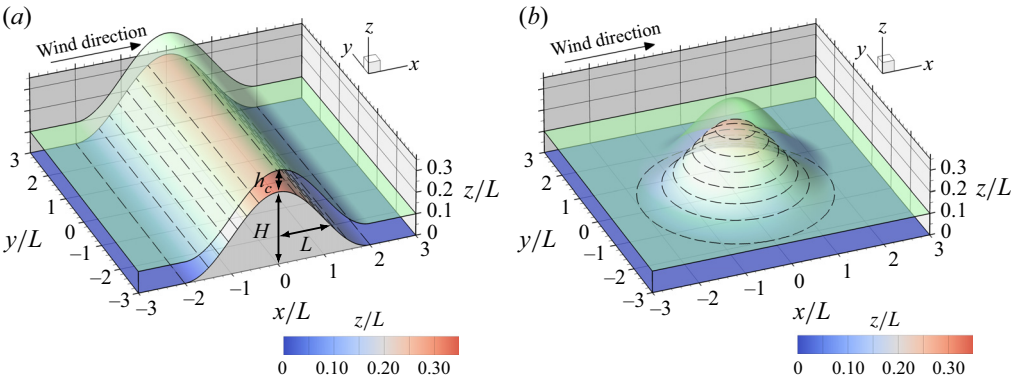

Figure 3. A zoomed presentation of the 2D (*a*) and 3D-axisymmetric (*b*) cosine hills interrogated. In (*a*), $L = L_x$ and L_y is not defined, and in (*b*) $L = L_x = L_y$. H is the hill height (3.2). The green surface depicts canopy top h_c.

Appendix B derives new formulae for h_i and h_m incorporating changes to the logarithmic mean velocity profile and the accompanying flux-gradient relationship which occur over a tall plant canopy (Harman & Finnigan 2007, 2008); labelled $\widehat{h}_m$ and $\widehat{h}_i$ using similar notation to Harman & Finnigan (2007, 2008). For the configurations discussed here, $\widehat{h}_m \sim (32.8, 21.7)$ m and $\widehat{h}_i \sim (11.8, 9.8)$ m for cases with $s_m = (0.16, 0.26)$, respectively, where these values represent their physical height above the origin of the above-canopy coordinates $z = d + z_o$ in the upwind flow (Appendix B). For reference, h_i for the current configuration using this same reference height is $\sim (9.3, 7.2)$ m, respectively, and $h_m = \widehat{h}_m$.

Secondly, figure 4 presents a regime diagram following that proposed by Poggi *et al.* (2008) that characterizes the simulations based upon key length scales determining canopy influences on the flow. The length scales of importance are the canopy height h_c, canopy
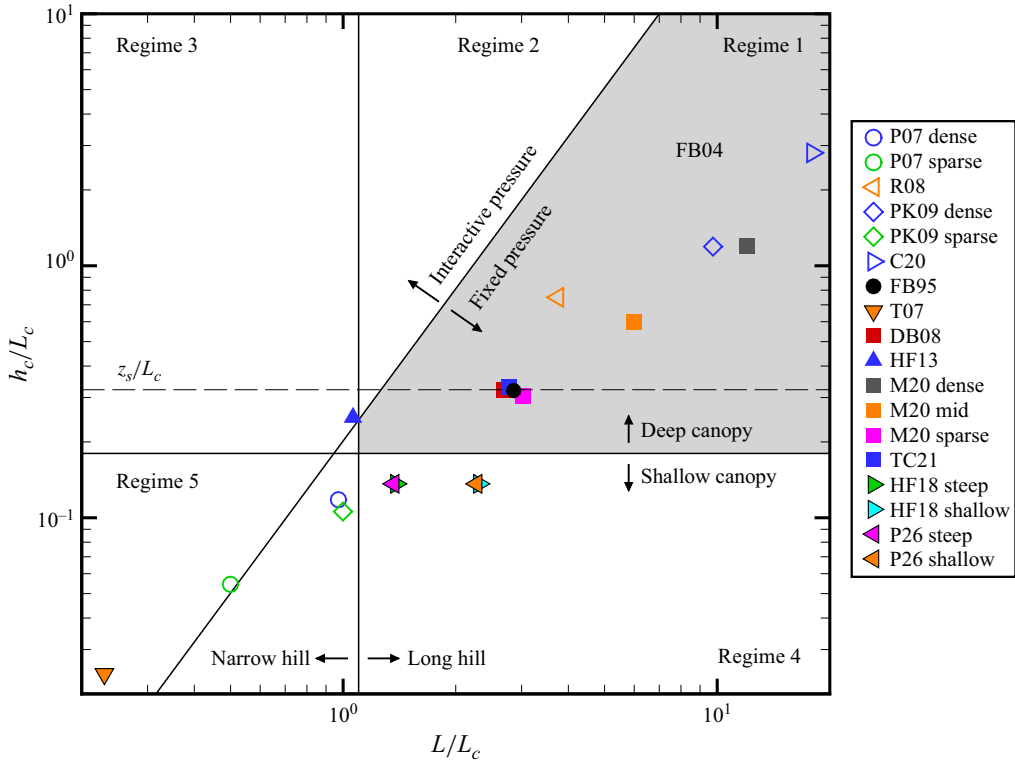
Figure 4. Length scale regime diagram following Poggi *et al.* (2008) mapping the hill geometry and canopy morphology of the current numerical (labelled P26) and WT (Harman & Finnigan 2018, HF18) simulations relative to previous research on turbulent flow over low forested hills. Here, low hills implies that $H/L \ll 1$ with H the hill height, and L the hill half-length at half the hill height. Here h_c is the canopy height, and L_c is the canopy adjustment length. Low hills with $L/L_c < 1.1$ are deemed 'narrow', and with $L/L_c > 1.1$ 'long'. Canopies with $h_c/L_c < 0.18$ are deemed 'shallow', and $h_c/L_c > 0.18$ 'deep', where $0.18 = 2\beta^2$ when $\beta = u_*/u|_{h_c} = 0.3$. From Finnigan & Belcher (2004, FB04), the envelope $h_c/L_c = 2(H/L)(L/L_c)^2$ delineates the regime in which the mean within-canopy vertical velocity is expected to be sufficiently large to affect the outer layer pressure. Previous research included Finnigan & Brunet (1995, FB95), Tamura *et al.* (2007, T07, where $\beta = 0.3$ is assumed), Poggi *et al.* (2007, P07), Dupont & Brunet (2008, DB08), Ross (2008, R08), Patton & Katul (2009, PK09), Harman & Finnigan (2013, HF13), Ma *et al.* (2020, M20), Chen *et al.* (2020, C20) and Tolladay & Chemel (2021, TC21). Open symbols reflect work on sinusoidally repeating low forested hills, and filled symbols reflect work on isolated forested hills. Symbols without a black outline study flow over low 2D forested hills (ridges), those with a black outline study flow over low 3D forested hills. The thin long-dash black line marks the canopy height at which one would expect separation z_s for the current canopy configuration according to FB04.

adjustment length L_c and the hill half-length at half the hill height L. Regime 1 marks the region where the Finnigan & Belcher (2004, FB04) theory is valid. In Regime 2, deviations from the FB04 theory can be attributed to within-canopy vertical velocities being of sufficient amplitude to alter the pressure in the inner layer above the canopy; i.e. when L/L_c is large, the canopy flow adjusts to the pressure gradient more rapidly than the pressure gradient changes (Belcher, Harman & Finnigan 2011). In Regime 3, such deviations can be attributed to both pressure and advection. In Regime 4, the canopy is insufficiently deep or dense to absorb all the momentum and hence within-canopy turbulence is influenced by finite shear stress at the underlying surface. All of these processes are at play for flows in Regime 5. Figure 4 shows that the current simulations

fall within Regime 4, a regime that falls outside the applicability of current theory (e.g. Finnigan & Belcher 2004; Harman & Finnigan 2009, 2013) and which has not received much attention in the literature.

The numerical and physical WT simulations differ in that a constant external pressure gradient ($\Pi_x = 1.63 \times 10^{-4} \, \text{m s}^{-2}$, selected to reproduce u_* observed in the tunnel) drives the flow in the x-direction in the LES, while the WT is a zero pressure-gradient tunnel. The flow sampled in the WT therefore represents an internal boundary layer driven by downward transport of momentum from the free stream airflow above, while the LES simulations represent a pressure-gradient driven fully developed boundary layer that is turbulent throughout the domain.

Another aspect of the numerical simulations that differs from the WT physical simulations is that the numerical simulations use periodic boundary conditions in the lateral direction, while the WT has viscous sidewall boundary layers. The horizontal dimensions of the numerical simulation domain are selected to ensure that the flow interacting with the 3D hills remains independent of the problem design. In the configuration with 3D hills (table 1), the hill only occupies a maximum of $\sim 3\%$ of the lateral domain that should ensure that any hill-induced flow perturbations are negligible at the lateral boundaries.

4. Analysis procedures

Analysis of the 2D- and 3D-hill simulations differ because the 2D simulations contain an homogeneous horizontal direction, i.e. the lateral (y) direction, while the 3D simulations do not. In the 2D-hill case, mean flow fields and higher moments are laterally averaged and time-averaged during the simulation and statistics are calculated during postprocessing. Analysis of the 3D simulations relies solely upon time averages (analogous to single-point WT measurements) based upon first-, second- and third-order moments calculated at every time step during the simulation. For the 2D-hill cases, a turbulent fluctuation is defined as a deviation from an instantaneous lateral average and higher moments are calculated as laterally averaged products which are then time-averaged over the duration of the simulation. For the 3D-hill cases, a turbulent fluctuation is defined as a deviation from a time-average at a single point and higher moments are calculated as time-averaged products of those fluctuations. The notation $\langle \rangle$ is used to denote a mean and a $'$ for a fluctuation from that mean.

To compare the numerical and WT simulations, all flow variables are normalized by time-averaged friction velocity u_* evaluated at canopy top ($z/h_c = 1$) and at $x/L = -4$, which is characteristic of the undisturbed flow approaching the hill. The actual u_* values derived from the simulations can be found in table 1, note that the small u_* variations shown in table 1 reflect a slight need for additional averaging. The simulations are currently averaged over 150 000 time steps (or, if we define a large-eddy turnover time τ_ℓ as the height of the domain (512 m) divided by the friction velocity u_*, 150 000 time steps is $\sim 8\tau_\ell$). Two characteristic length scales are used: (i) the length of the hill at half its height in the along-wind direction L, and (ii) the canopy height h_c.

5. Comparison with WT measurements

5.1. *Flow fields*

For the 3D–hill cases, vertical profiles of mean wind speed from the LES agree quite well with the WT observed profiles (figure 5). Minor differences can be seen at $x/L = -1$ and $x/L = 0$, i.e. halfway up the hill and at hill-crest, where the LES produces slightly
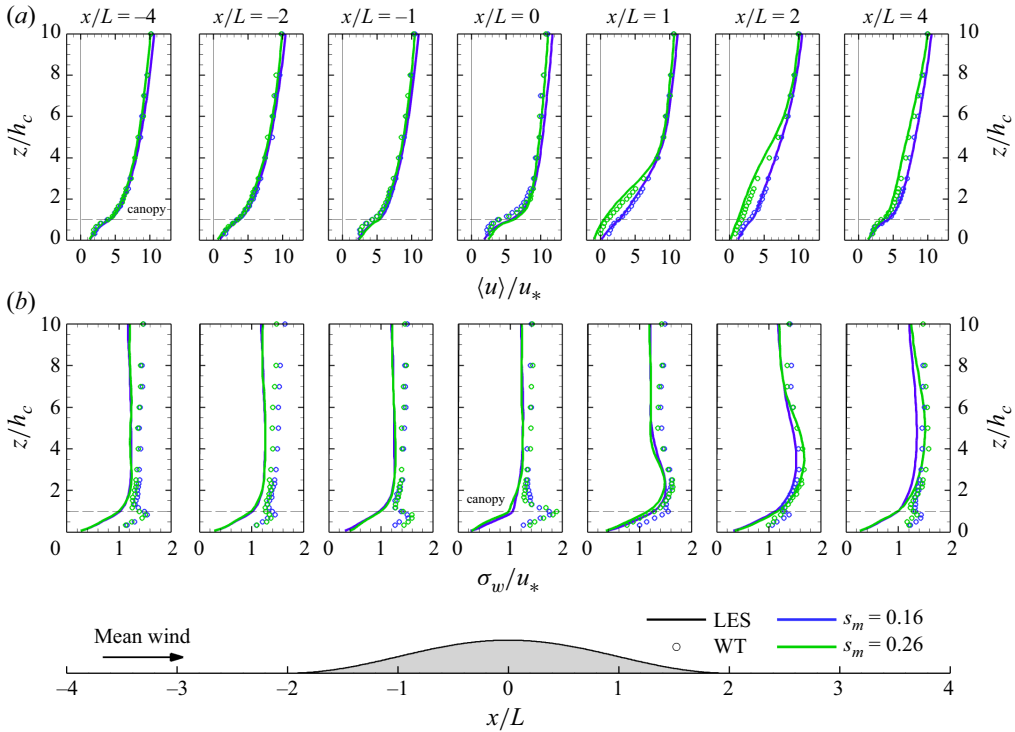
Figure 5. A comparison of WT observed (symbols) and numerically simulated (lines) vertical profiles of average streamwise velocity, u (*a*), and vertical velocity standard deviation, σ_w (*b*), at hill centreline over axisymmetric hills normalized by the friction velocity u_*. Blue colours reflect results for the case with $s_m = 0.16$, and green colours reflect results for the case with a slope $s_m = 0.26$; for the LES the data are from 3D–0.16 and 3D–0.26, respectively. The mean flow direction in these figures is from left to right (in the $+x$ direction). In these figures, we are using a coordinate system that is aligned with (and perpendicular to) the flat terrain surrounding the hill, so positive u is in the $+x$ direction, and positive w is upward.

higher wind speeds in the upper canopy. Vertical profiles of the vertical velocity standard deviation ($\sigma_w = \langle w'^2 \rangle^{1/2}$) reveal larger differences between simulations and observations, but the overall trend of the evolution over the hill match well. The most noticeable difference in σ_w occurs inside the canopy. These differences can be attributed to the fact that the WT measurements represent samples at fixed locations within the rod canopy, and hence the measurements sample the wakes that waver horizontally and vertically in the lee of the individual physical canopy elements in response to turbulent motions at scales larger than the canopy element spacing. In contrast, the canopy-resolving LES parametrizes the average influence of all canopy elements within a grid cell and hence do not resolve any individual physical canopy elements or the turbulence comprising their wake. Harman *et al.* (2016) demonstrated substantial variability of 80 individual σ_w profiles collected within a single interelement volume; σ_w profiles averaged over all 80 profiles largely eliminates the within-canopy σ_w peaks, thereby appearing more like those produced by the LES. Harman & Finnigan (2018) conducted similar sampling of 16 locations surrounding a single peg of the current canopy at $x/L = -4$; Appendix A shows that observed σ_w/u_* averaged over these 16 locations still peaks in the upper canopy, but the peak is clearly reduced compared with the single-point statistics presented in figure 5 and is more like that in the LES. Therefore, if the WT measurements were to have collected vertical profiles throughout the entire inter-rod volume, notably better agreement would be expected for
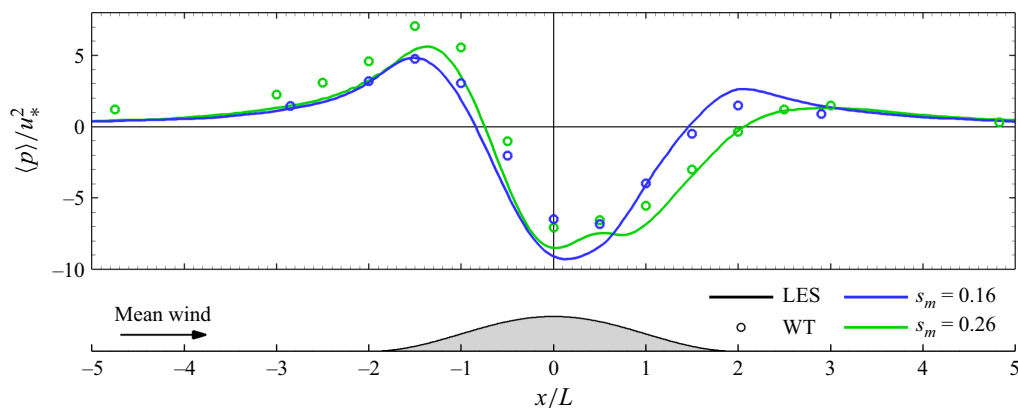
Figure 6. A comparison streamwise transects of normalized surface pressure variations at hill centreline normalized by u_*^2 for 3D forested hills of two slopes ($s_m = 0.16$ (blue colours) and 0.26 (green colours)); for the LES, these results are from cases 3D–0.16 and 3D–0.26, respectively. Solid lines represent LES results, and symbols reflect the WT measurements.

σ_w between the WT and the LES. Nevertheless, these comparisons provide substantial evidence that the LES reasonably reproduces the physical simulations.

5.2. *Pressure*

In the absence of a canopy, the surface pressure perturbation induced by neutral flow encountering an isolated obstruction exhibits an initial peak associated with flow stagnation on the upwind side of the obstruction, a pressure minimum at the hill crest resulting from the flow acceleration over the hill, followed by a second pressure peak on the hill's leeward side as the flow moving over the hill encounters the flat surface again and then recovers downwind of the hill to its undisturbed upwind state (e.g. Jackson & Hunt 1975; Hunt *et al.* 1988). Theory suggests that because canopies interact with the flow through pressure, that the presence of vegetation on hills can shift the pressure distribution sufficiently to make forested hills appear steeper than one would anticipate (e.g. Finnigan & Belcher 2004). Asymmetries in and phase shifts of the surface pressure perturbations relative to the hill define the orographic surface drag felt by the flow and dictate whether flow separation will occur on leeward slopes (e.g. Belcher *et al.* 2011). Therefore, the surface pressure distribution reflects the overall hill- and canopy-induced influence on the flow and represents a key metric whose accuracy needs to be demonstrated.

During the WT experiments, a manifold system sampled the surface pressure via tubes inserted into holes drilled into the hill surface (Harman & Finnigan 2018). Comparing observed and simulated along-wind surface pressure variations normalized by u_*^2 at hill centreline (figure 6) reveals broad overall agreement between the WT and the LES of the location and phasing of the pressure maxima and minima for both hill slopes. On the windward side of the hill, the pressure peak in the steep hill case is of slightly higher magnitude in the WT than in the LES, while the pressure minima near hill-centre or just downwind of the crest is of higher magnitude in the LES than the WT; which, in combination implies a slightly larger surface pressure gradient driving the flow in the LES producing the slightly higher in-canopy wind speeds shown in figure 5. These features likely result from our decision for the LES simulations to target outdoor situations and the associated taller LES domain compared with the depth of the boundary layer in the WT, but do not negatively influence confidence in the LES solutions.
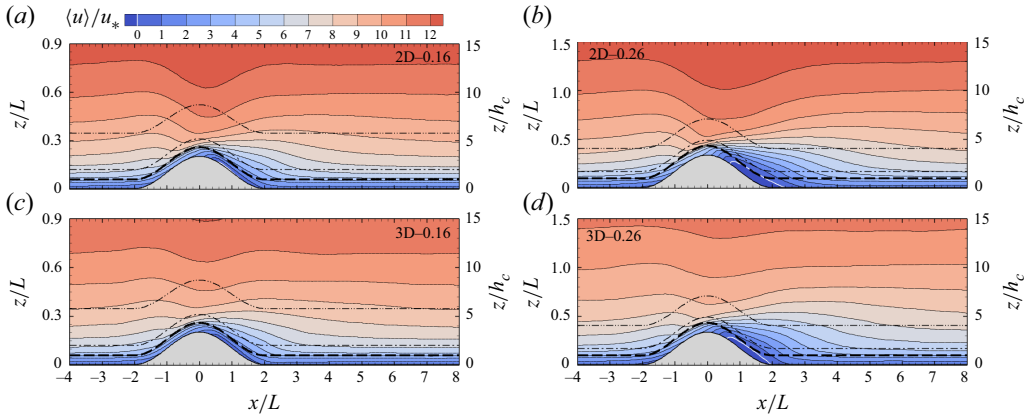
Figure 7. Vertical slices of average streamwise velocity $\langle u \rangle$ normalized by the friction velocity u_*. Panels (*a*) and (*c*) present results from the shallow-sloped hills ($s_m = 0.16$), and panels (*b*) and (*d*) from the steeper hills ($s_m = 0.26$). Panels (*a*) and (*b*) present time-averaged and laterally averaged 2D-hill results, panels (*c*) and (*d*) present time-averaged 3D-hill results. In all figures, the dashed black line depicts canopy top. All four figures use the same vertical axis relative to the canopy height (h_c), which means that they're presented up to different heights relative to the hill half-length (L). The mean wind flow is from left to right (in the $+x$ direction). The white contour line marks zero streamwise velocity. The dash–dot line is ζ_i / h_c, and the dash–dot–dot line is ζ_m / h_c; see § 7 for definition of ζ_i and ζ_m.

The results presented in figures 5 and 6 provide evidence that the LES and its configuration accurately simulates turbulent flows over isolated 3D hills. Therefore, the LES results can now offer insight into aspects of flow over 2D or 3D forested hills that are difficult to observe.

6. Flow over 2D versus 3D forested hills

Flow over isolated hills differs from flow over repeating 2D cosine hills, because in the latter the flow approaching any single hill feels the influence of the hill just upstream and all previous hill adjustments (e.g. Belcher *et al.* 1993). Turbulent flow over isolated 2D and 3D hills differ substantially due to the ability for the flow to leak around the sides of 3D hills (e.g. Mason & King 1985). We now interrogate mean variations in the flow fields resulting from interactions with isolated 2D and 3D forested hills.

6.1. *Mean wind*

Figure 7 shows the influence of hill-shape and hill-slope on the vertical variation of mean streamwise velocity. It is important to recall that figure 7(*a,b*) present *y*- and time-averaged 2D *x*–*z* slices, while figure 7(*c,d*) show time averages at hill centreline ($y/L = 0$). It is also important to recall that flow variables (u, v, w) represent flow in the (x, y, z) directions.

For the steeper hills ($s_m = 0.26$), a separation bubble forms on the hill's leeward side within the canopy for both hill-shapes (figure 7), where reverse flow spans the region between $0.67 < x/L < 2.29$ ($0.67 < x/L < 1.93$) and extends vertically through the entire (most of the) canopy depth in the 2D (and 3D) cases, respectively. Flow separation also occurs intermittently over the shallower-sloped hills ($s_m = 0.16$), but mean separation is only found in 2D–0.16 confined to regions very close to the surface and to $0.56 < x/L < 1.25$. All cases reveal a within-canopy speed-up on the windward side of the hill occurring between approximately $-1.5 \leq x/L \leq -0.5$. At a fixed height above the trees (e.g. $z/h_c = 10$), cases with shallower-sloped hills ($s_m = 0.16$, figure 7*a,c*) result in higher
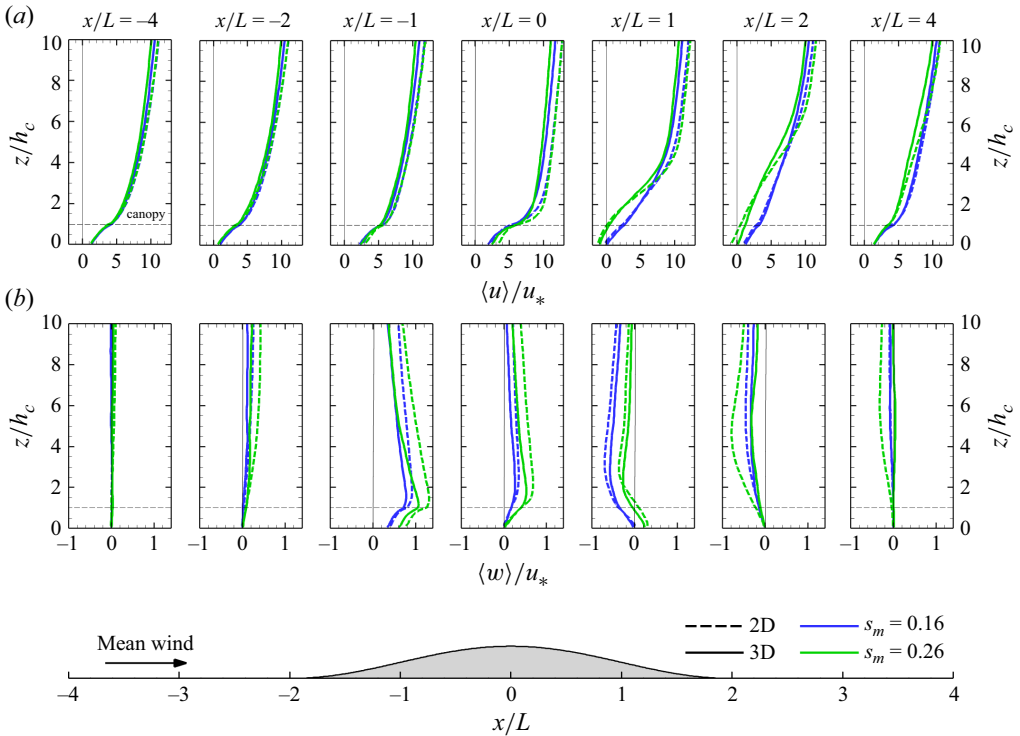
Figure 8. Vertical profiles of average streamwise (*a*) and vertical (*b*) velocity normalized by the friction velocity u_* comparing the four cases. Dashed lines depict results for flow over the 2D hills, and solid lines depict results over 3D hills at hill centreline ($y/L = 0$). Flow over the shallow-sloped hills ($s_m = 0.16$) are in blue, and flow over the steeper hills ($s_m = 0.26$) are in green. The mean wind flow is from left to right (in the $+x$ direction).

average streamwise wind speeds for the same imposed pressure gradient compared with those with steeper hills (figure 7*b*,*d*). A direct comparison of the 2D versus 3D flow fields at specified locations (figure 8) emphasizes these findings quantitatively. Overall, 2D-hills induce larger amplitude streamwise $\langle u \rangle$ and vertical velocity $\langle w \rangle$ than do 3D hills, especially above the canopy; this result should be expected due to the ability for the flow impinging on the hill to leak around the sides of the 3D hills. At the foot of the windward side of the hill ($x/L = -2$), all cases display non-zero $\langle w \rangle$ suggesting that the flow already feels the hill-induced pressure forces. At $x/L = -1$, $\langle w \rangle$ at canopy top increases by nearly 11 % for 2D compared with 3D hills for cases with $s_m = 0.16$, compared with a 19 % increase for cases with $s_m = 0.26$. At hill-crest, $\langle w \rangle$ remains upward above and within the upper canopy. Canopy-top wind speeds are highest in the region between $x/L = -1$ and 0, but the largest vertical gradient in streamwise velocity is found near $x/L = 0$. Reverse flow within the canopy is clearly apparent at $x/L = 1$ for the cases with $s_m = 0.26$, i.e. negative streamwise velocity and positive vertical velocity within the canopy with both changing sign at canopy top. The 2D hill case with $s_m = 0.26$ clearly requires a longer distance downwind for $\langle w \rangle / u_*$ to relax back to conditions upwind wind of the hill, which has not occurred by $x/L = 4$. In combination, the profiles in figure 8 demonstrate the increased role of mean vertical advection of streamwise momentum with increasing hill slope whose sign varies with position on the hill, and emphasize that care should be taken when comparing the current simulation results (where flow variables are presented in a coordinate system aligned with the upstream flat surface) and outdoor field measurements
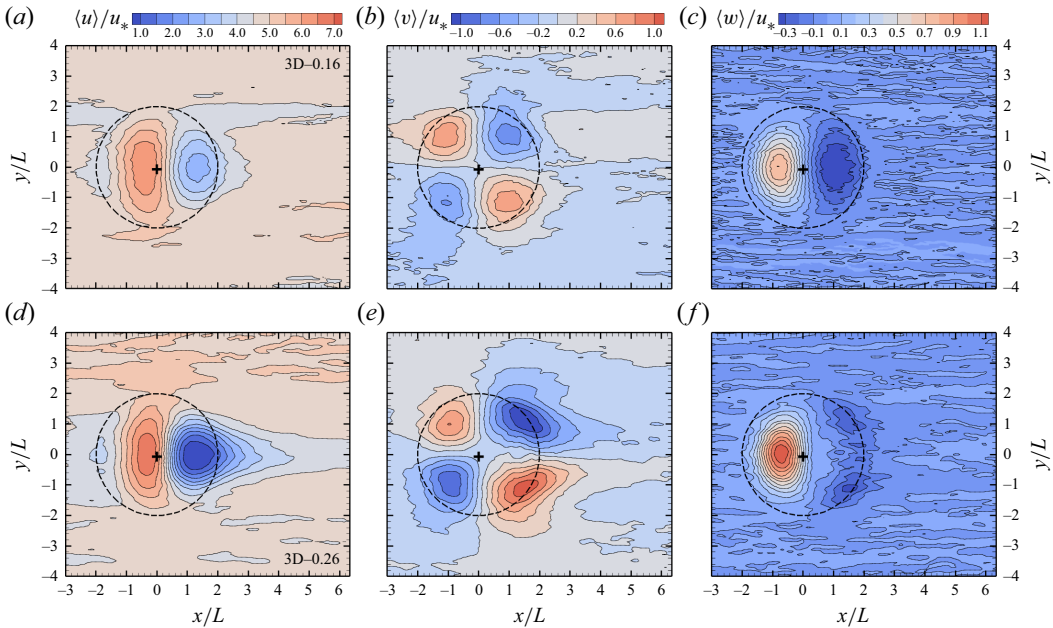
1026 A16-16

Figure 9. Horizontal terrain-following (at constant ζ) slices of time-averaged streamwise velocity, $\langle u \rangle$ (a,d), and spanwise velocity, $\langle v \rangle$ (b,e), and vertical velocity, $\langle w \rangle$ (c,f), at canopy top $(\zeta / h_c \sim 1)$ normalized by u_* from the two 3D-hill simulations: $(a–c)$ 3D–0.16; $(d–f)$ 3D–0.26. The dashed black line depicts the location of the hill base at $\zeta / L = 0$, and the black cross marks the hill-crest. The mean wind flow is from left to right (in the $+x$ direction).

that rotate variables into a flow-dependent coordinate system forcing local $\langle w \rangle$ to zero (e.g. Wilczak, Oncley & Stage 2001; Finnigan *et al.* 2003; Finnigan 2004).

Figure 9 shows terrain-following horizontal surfaces of $\langle u \rangle$, spanwise $\langle v \rangle$ and vertical $\langle w \rangle$ velocity normalized by u_* at canopy-top $(z / h_c \sim 1)$ for the two 3D-hill cases and demonstrates the horizontal variability of mean wind fields induced by variations in hill-slope. Figure 9(a,d) show that increased hill slope dramatically increases the speed-up on the windward side and a slow-down on the leeward side. Maximum wind speeds at canopy-top occur on the windward side of the hill at approximately $x/L = -0.3$ (see $\mathrm{max}(\Delta u/u_b)_{h_c}$, table 1), and extend laterally to approximately $y/L = 1$, while the peak wind-speed reduction at canopy-top on the leeward side occurs at approximately $x/L = 1.5$ and only extends laterally to approximately $y/L = 1$. Note that these results differ from those in turbulent flow over unforested hills where the maximum speedup occurs at the hill-crest (e.g. Jackson & Hunt 1975; Ayotte & Hughes 2004); Finnigan & Belcher (2004) present an explanation describing the canopy-imposed mechanisms controlling this shift for flow over 2D-hills. With increasing hill steepness, maximum speedup at canopy top and at hill centreline increases and shifts up slightly downwind $(\mathrm{max}(\Delta u/u_b)_{h_c}$, table 1).

Figure 9(b,e) demonstrate the horizontal distribution of the mean lateral velocity v at canopy top induced by the 3D hills. Increased hill-slope also increases the magnitude of the hill-induced lateral velocity, with lateral velocities on the windward side of the hill ($x/L < 0$) generally of lower magnitude than those on the leeward side ($x/L > 0$). For both hill slopes, the lateral velocities are induced out to lateral regions approximately $y/L = \pm 3$ (as defined by $\langle v \rangle/u_* > \pm 0.2$). In the case with $s_m = 0.16$, lateral velocities largely disappear by $x/L = 2$, while the flow encountering the steeper hill ($s_m = 0.26$), lateral velocities at canopy top persist downwind of the hill to at least $x/L = 4$. At the canopy top, the peak

hill-induced upward $\langle w \rangle / u_*$ is found along the windward hill centreline at $x/L \simeq -0.75$ for both 3D-hill cases (figure 9c,f), with the steeper hill ($s_m = 0.26$) generating a $\sim 40\,\%$ larger upward vertical velocity. Peak downward $\langle w \rangle / u_*$ at canopy top is found on the leeward side of the hills, with a single peak in the unseparated 3D–0.16 case along hill centreline at $x/L \simeq 1$, and a $\sim 23\,\%$ lower amplitude double peak in the separated 3D–0.26 case located at $x/L \simeq 1.5$ and $y/L \simeq \pm -1$.

In the 3D hill cases, the canopy's presence produces interesting lateral flow within the canopy (figure 10, showing spanwise vertical slices of v at three different x/L locations for the case with $s_m = 0.26$). On the upwind side of the hill (figure 10a), the hill induced stagnation pressure (to be further discussed in § 6.2) produces diverging lateral flow out to approximately $y/L = \pm 3$ and vertically throughout the canopy and up to heights of approximately $z/L = 1$ ($z/h_c = 10$). At hill centreline ($x/L = 0$, figure 10b), the above canopy flow continues its divergent path around the hill. However, canopy drag sufficiently reduces the streamwise velocities within the canopy that the hill-induced lateral pressure gradients produces within-canopy uphill flow on either side of the 3D hill. This convergent within-canopy flow starts at lateral distances of at least $y/L = \pm 3$. At $x/L = 1$ (figure 10c), the lateral flow converges in the hill's lee but over a shallower depth than is the divergent flow on the hill's windward side. Similar lateral flow features are also found in the WT (Harman & Finnigan 2018). This hill-induced within-canopy lateral flow likely has significant impact on the transport of surface- and canopy-emitted scalars and hence the interpretation of single-point scalar flux measurements in forested hilly terrain.

6.2. *Pressure*

Axisymmetric 3D hills produce slightly higher stagnation pressure peaks on the windward side of the hill, and notably reduced negative pressure near the hill crest compared with 2D hills (figure 11 and figure 12a,d). This feature results from the impinging flow leaking around the lateral sides of the 3D hill compared with the 2D hill which produces more blockage as the flow is forced to go over the hill, hence 2D hills produce higher magnitude canopy-top wind speeds overall ($\mathtt{max}(\Delta u / u_b)_{h_c}$, table 1). For both hill shapes, steeper hills ($s_m = 0.26$) shift the pressure minima more towards the hill crest compared with the shallower sloped hills ($s_m = 0.16$), but also broaden the along-wind region containing the minimum such that the lowest pressures span a region from approximately $-0.5 \le x/L \le 1.5$ (compared with $-0.2 \le x/L \le 0.9$ in the cases with shallower-sloped hills). Of note, however, is the secondary pressure minima in the hill lee in both the 2D–0.26 and the 3D–0.26 simulations (perhaps best seen in figure 13), a feature which has not been mentioned in previous studies of turbulent flow over forested hills and which therefore likely arises from the shallow canopy (Regime 4, figure 4) and its influence on flow separation.

Figure 12(b,e) and 12(c,f) present horizontal surfaces (constant ζ) of the streamwise and spanwise pressure gradient induced by the 3D hills; these four panels show results at midcanopy height ($\zeta / h_c \sim 0.6$) rather than at the surface like that in figure12(a,d). Clearly, the induced streamwise pressure gradient achieves larger amplitudes in the streamwise direction than in the spanwise direction. Compare $\mathtt{max}((\partial \langle p \rangle / \partial x)\,(h_c / u_*^2)) \sim (0.77, 1.56)$ and $\mathtt{min}((\partial \langle p \rangle / \partial x)\,(h_c / u_*^2)) \sim (-0.64, -0.86)$, respectively, for $s_m = (0.16, 0.26)$, and for the spanwise direction for which the maxima/minima are symmetric, with $\mathtt{max/min}((\partial \langle p \rangle / \partial y)\,(h_c / u_*^2)) \sim \pm(0.36, 0.59)$ for $s_m = (0.16, 0.26)$, respectively. Although the spanwise pressure gradients are of lower magnitude from that in the streamwise direction, the lateral uphill in-canopy flows seen in figure 10 in the case with $s_m = 0.26$ at $x/L = 0$ suggest that the hill-induced spanwise pressure gradient is of sufficient magnitude to dominate downward transport of momentum down into the
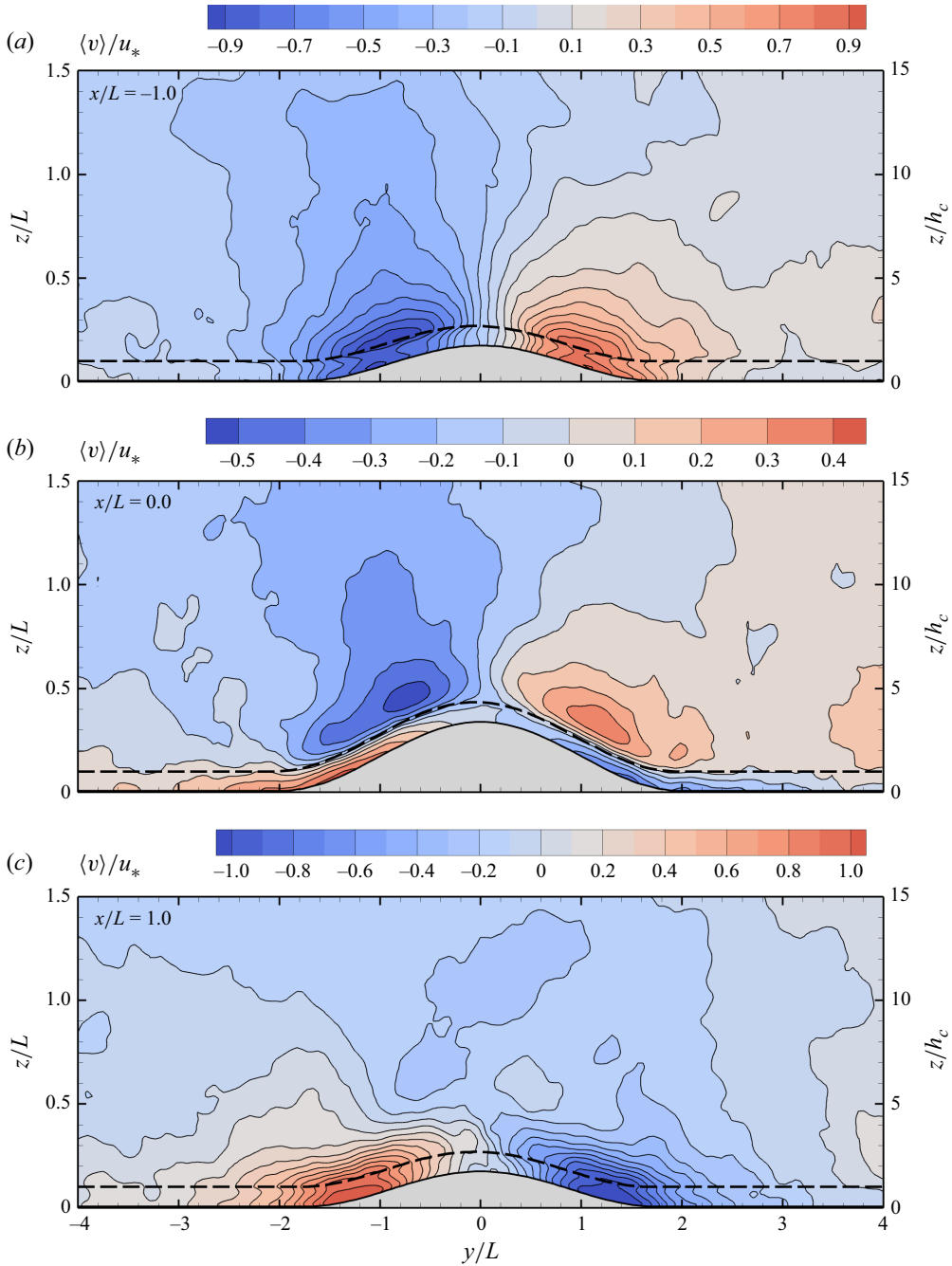
Figure 10. Spanwise vertical slices (y–z) of time-averaged spanwise velocity v normalized by u_* at three along-wind locations: (a) $x/L = -1$; (b) $x/L = 0$; (c) $x/L = 1$) from 3D–0.26. Positive v is in the $+y$ direction. The dashed black line depicts canopy top ($z/h_c = 1$). The mean streamwise wind flow is out of the page (in the $+x$ direction). Note that contour ranges and intervals differ between panels.
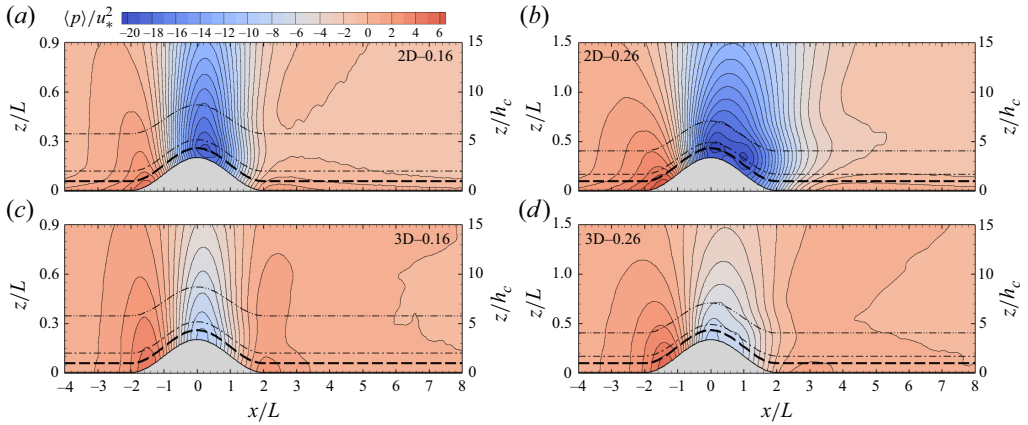
Figure 11. Vertical slices of average pressure normalized by the friction velocity u_*^2. Panels (a) and (c) present results from cases with shallow-sloped hills ($s_m = 0.16$), and panels (b) and (d) from cases with steeper hills ($s_m = 0.26$). Panels (a) and (b) present time-averaged and laterally averaged 2D-hill results, panels (c) and (d) present time-averaged 3D-hill results at hill-centreline. In all panels, the heavy dashed black line depicts canopy top, the dash–dot line ζ_i / h_c, and the dash–dot–dot line ζ_m / h_c (see § 7). All four panels use a consistent vertical axis relative to canopy height (h_c), which means that they are presented up to different heights relative to the hill half-length (L). The mean wind flow is from left to right (in the $+x$ direction).

canopy along the sides of the 3D hills. Compared with the case with $s_m = 0.16$, the case with $s_m = 0.26$ also shows strong lateral pressure gradients downwind of hill crest, but concentrated primarily in regions out towards hill-base.

Figure 13(a) shows a comparison of the horizontal variation of normalized surface pressure along the hill-centreline for the four cases. Figure 13(b) shows the correlation between the mean hill-induced surface pressure perturbations $\langle p \rangle$ and the local hill slope h_x, where the integral under these curves represent the pressure drag in the x direction at hill centreline (see F_p in table 1). In all cases as the flow approaches the hill (from left to right in the figure), it first feels a pressure force retarding the flow (e.g. stagnation, positive $\langle p \rangle h_x$); an increase of 10 % in hill slope increases the pressure force in this region by approximately a factor of four. The amplitude and streamwise horizontal region over which this force acts also evolves with variations in hill-shape; where for 2D hills this retarding force acts over a smaller horizontal extent than it does for 3D hills, and the horizontal extent over which this retarding force acts increases with increasing hill-steepness. At a location somewhere between $-1.1 \leq x/L \leq -0.7$, pressure drag changes sign to become an accelerating force (e.g. a thrust, negative $\langle p \rangle h_x$). Again, the spatial region over which this thrust acts on the flow increases with increasing hill steepness, however, the horizontal extent over which it acts decreases as the hills change from a 2D ridge to an axisymmetric 3D hill. Pressure drag acts to retard the flow (positive $\langle p \rangle h_x$) across nearly the entire leeward side of the hill for all cases, with the exception of a small region of acceleration (thrust) that develops in the cases with shallower slopes (i.e. between $1.5 \lesssim x/L \leq 2$). The region of maximum pressure drag on the leeward side shifts downstream with increasing hill steepness.

Consistent with Ross & Vosper (2005) and Poggi & Katul (2007a,b), peak minimum pressure is generally found at or just downstream of hill crest ($0 \lesssim x/L \lesssim 0.5$), however, both of the $s_m = 0.26$ cases interestingly show a surface pressure increase at $0.5 \lesssim x/L \lesssim 0.6$ not present in either of the $s_m = 0.16$ cases (figure 13a). 2D–0.16 in figure 11 shows a similar pressure increase in the midcanopy and above, suggesting that this pressure
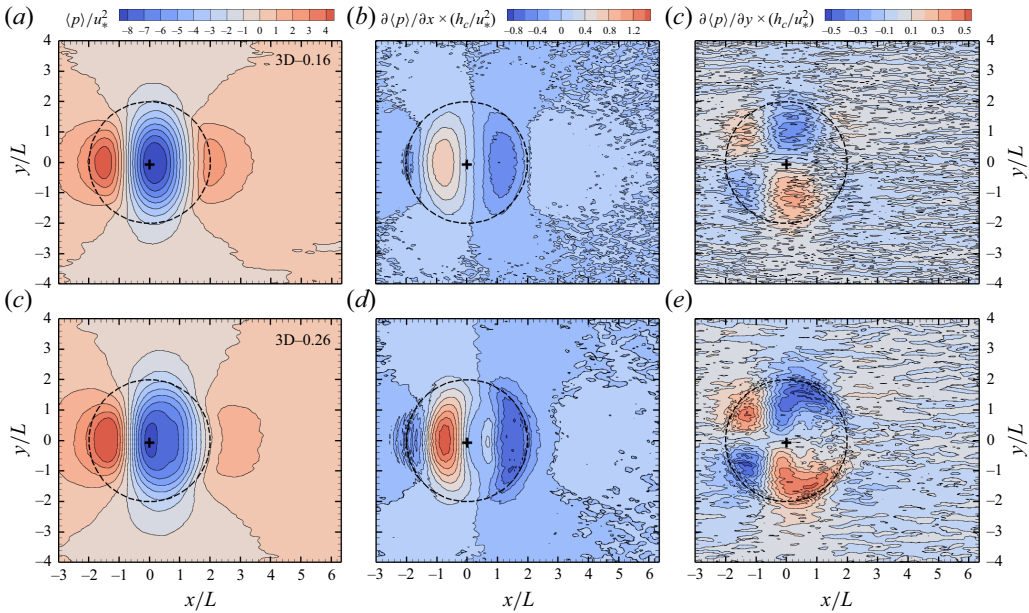
Figure 12. Horizontal terrain-following surfaces of time-averaged surface pressure, $\langle p \rangle$ (a,d), streamwise pressure gradient, $(\partial \langle p \rangle / \partial x)$ at $\zeta / h_c \sim 0.6$ (b,e) and spanwise pressure gradient $(\partial \langle p \rangle / \partial y)$ at $\zeta / h_c \sim 0.6$ (c,f) from the two 3D-hill simulations, normalized by appropriate combinations of u_*^2 and h_c. Panels $(a$–$c)$ depict results from 3D–0.16, and $(d$–$f)$ from 3D–0.26. The dashed black line depicts the location of the hill base at $\zeta / L = 0$, and the black cross marks the hill-crest. The mean wind flow is from left to right (in the $+x$ direction).
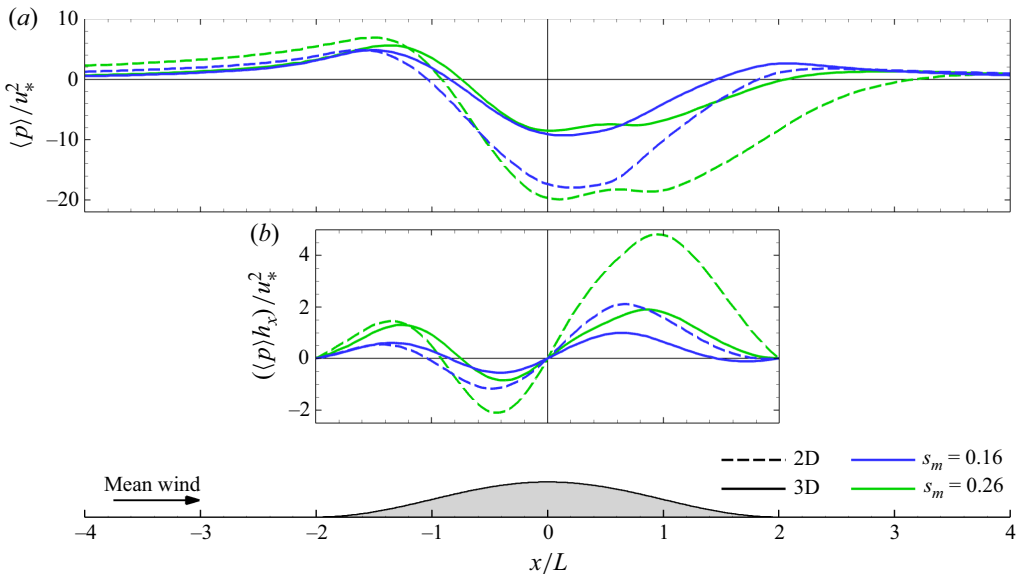

Figure 13. (a) A comparison of surface pressure $(\langle p \rangle)$ over 2D (dashed lines) and 3D (solid lines) hills. Hills with $s_m = 0.16$, blue lines; and with $s_m = 0.26$, green lines. Note that the solid lines in this panel are the same as those in figure 6. (b) A comparison of the negative correlation between the pressure distributions shown in (a) and the local hill slope $(h_x = \partial h / \partial x)$ at hill centreline normalized by u_*^2 for all simulations; i.e. the longitudinal variation of the hill- and canopy-induced pressure drag, where positive (negative) values represent a force acting to decelerate (accelerate) the flow, respectively. Results in both panels are laterally averaged for cases with 2D hills, and time-averaged along hill-centreline for cases with 3D hills.
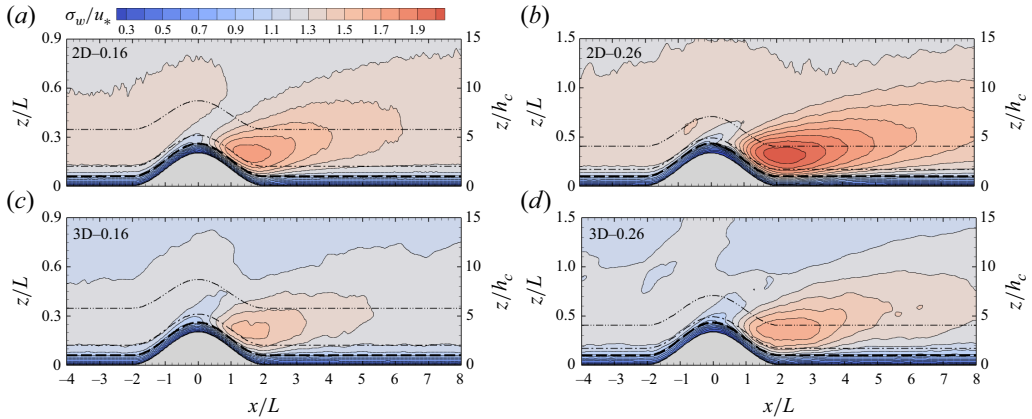
Figure 14. Vertical slices of the average standard deviation of vertical velocity σ_w normalized by u_* from all four simulations. Same layout as for figure 7. The mean wind flow is from left to right (in the $+x$ direction).

increase might result from an interaction of canopy processes and the hill-induced large scale pressure field. Figure 8 also shows that the mean flow reverses in the lower-canopy to midcanopy in the region $1 \lesssim x/L \lesssim 2$. Therefore, this secondary pressure peak might result from the stagnation associated with the positive within-canopy streamwise velocity $\langle u \rangle / u_*$ at $x/L = 0$ and the reversed streamwise flow at $x/L = 1$. This secondary pressure increase in the lee of steeper $s_m = 0.26$ hills for flows in Regime 4 contradicts Poggi & Katul's (2007a) suggestion to estimate hill-induced pressure perturbations based upon the effective (or apparent) surface determined by the windward terrain surface and the leeward separation bubble.

6.3. *Turbulence*

All cases generate an increase in the normalized standard deviation of vertical velocity σ_w/u_* on the leeward side of the hill (figure 14) resulting from the hill-induced elevated shear layer in the hill's lee. Generally, this leeward increase of σ_w/u_* is of larger magnitude in the 2D hill cases (figure 14a,b) than in the 3D hill cases (figure 14c,d) with peak values of approximately 1.6 in the lower sloped case ($s_m = 0.16$) over the region between $1 < x/L < 2$ for both the 2D and 3D hills, while for the steeper hills ($s_m = 0.26$) σ_w/u_* peaks at approximately 1.9 over the region spanning approximately $1 < x/L < 3$; accentuated vertical velocity fluctuation amplitudes persist downwind to well beyond $x/L = 8$ (or $x/h_c = 80$) and extend vertically up to heights above $z/L = 1.2$ (or $z/h_c = 12$) with the maximum change in σ_w at canopy top $\Delta\sigma_{w_{h_c}}$ occurring at $x/L \sim 0.8$ for flow over the hills with $s_m = 0.16$ and at $x/L \sim (2.3, 1.3)$ for the (2D, 3D) hills with $s_m = 0.26$ (table 1).

The streamwise variation of vertical profiles of turbulent flow statistics along hill centreline help quantify the influence of hill shape and steepness (figure 15). Upwind of the hill ($x/L \sim -4$), (σ_u, σ_w)/u_* above canopy-top match their theoretically expected (e.g. Lumley & Panofsky 1964) values $\sim$(2.3, 1.3), respectively, and $\langle u'w' \rangle / u_*^2$ is nearly constant with height at a value of -1. Work performed by the flow against canopy drag ensures that turbulence moments diminish rapidly with descent into the canopy, similar to that found in the vicinity of numerous other canopies (e.g. Raupach 1994). On the windward side of the hills ($x/L \sim -1$), σ_u/u_* and σ_w/u_* change little at canopy top with the increased streamwise velocity increases shown in figures 8 and 9, however, the decreased vertical gradient in the streamwise wind at this x/L does manifest in
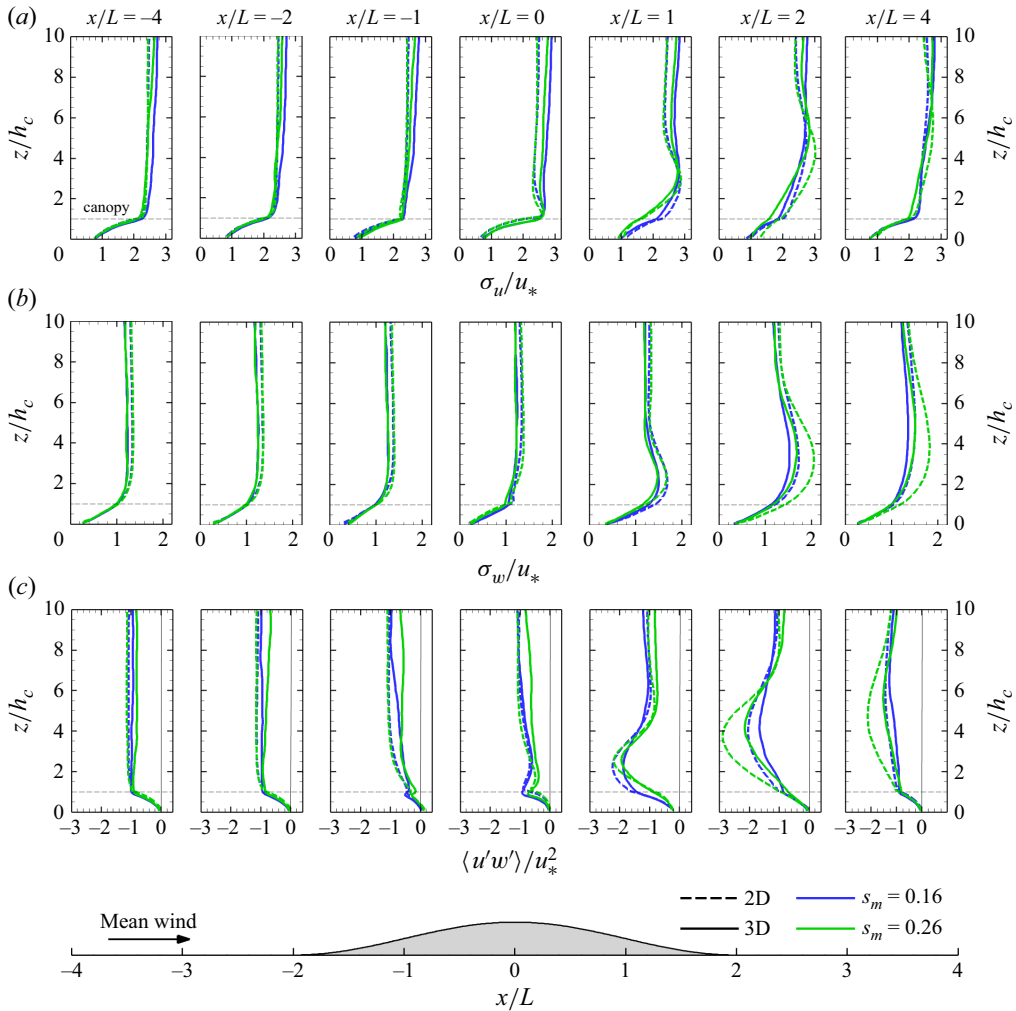
Figure 15. Vertical profiles of the standard deviation of streamwise velocity (*a*) and vertical velocity (*b*) normalized by the friction velocity u_* comparing the four cases at $x/L = (-4, -2, -1, 0, 1, 2, 4)$. Panel (*c*) presents vertical profiles of the vertical flux of streamwise momentum $\langle u'w' \rangle$ normalized by u_*^2 at the same x/L locations. Dashed lines depict results for flow over the 2D hills, and solid lines depict results over 3D hills at hill centreline ($y/L = 0$). Flow over the shallow-sloped hills ($s_m = 0.16$) are in blue, and flow over the steeper hills ($s_m = 0.26$) are in green. The mean wind flow is from left to right (in the $+x$ direction).

reduced momentum stress in the canopy's vicinity – with a greater amplitude reduction of $\langle u'w' \rangle / u_*^2$ near canopy-top in the cases with 3D hills compared with 2D hills sufficient to create a $\langle u'w' \rangle / u_*^2$ minimum just above the canopy. The steeper hills ($s_m = 0.26$) also reveal a very small region of weak near-surface upward turbulent momentum flux beneath canopy-top driven by the thrust force found in this region (figure 13). At hill-crest ($x/L = 0$), increased vertical shear of streamwise velocity amplifies σ_u / u_* and $\langle u'w' \rangle / u_*^2$ compared with their upstream values at $x/L = -4$, while σ_w / u_* diminishes slightly. On the hill's leeward side ($x/L = 1$ and $x/L = 2$), the hill- and canopy-induced adverse pressure gradient reduces mean streamwise velocity producing enhanced shear up to at least $z/h_c = 4$ which amplifies all three second moments throughout this depth compared with their upstream values (figure 15). At $x/L = 1$ just above the canopy, σ_u / u_* and
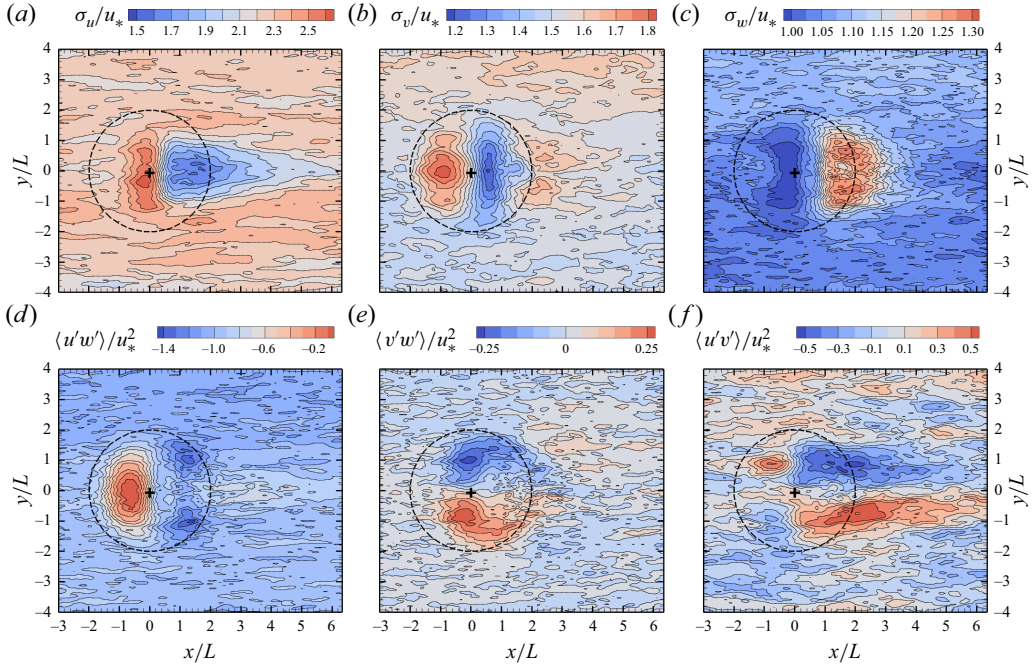
Figure 16. Horizontal slices of time-averaged velocity standard deviations normalized by u_* (a–c) and momentum flux normalized by u_*^2 (d–f) along the $\zeta/h_c = 0.95$ surface (i.e. near canopy top) from the steeper ($s_m = 0.26$) 3D hill simulation, 3D–0.26. In (a)–(c), results are presented for streamwise velocity, σ_u (a,d), spanwise velocity, σ_v (b,e), and vertical velocity, σ_w (c,f), and in (d)–(f) results are presented for vertical flux of streamwise momentum, $\langle u'w' \rangle$ (d), vertical flux of spanwise momentum, $\langle v'w' \rangle$ (e), and spanwise flux of streamwise momentum, $\langle u'v' \rangle$ (f). The dashed black line depicts the location of the hill base at $\zeta/L = 0$, and the black cross marks the hill-crest. The mean wind flow is from left to right (in the $+x$ direction).

$\langle u'w' \rangle / u_*^2$ increase most in the shallower hill cases ($s_m = 0.16$) where the flow does not separate no matter the hill shape. Within the broader hill-induced shear layer in the hill lee, flow over 2D hills amplifies σ_w/u_* and $\langle u'w' \rangle / u_*^2$ more-so than over 3D hills as the turbulence acts to counter the adverse pressure gradient. By $x/L = 4$, σ_u/u_* has nearly recovered its upstream profile, but not σ_w/u_* and $\langle u'w' \rangle / u_*^2$ – especially for cases with steeper hills ($s_m = 0.26$).

To elaborate on a 3D hill's influence on turbulence, figure 16 presents the spatial variation of turbulence moments along a constant ζ-surface at canopy top in the steeper ($s_m = 0.26$) 3D-hill simulation. On the windward side, pressure gradients induced by the steeper ($s_m = 0.26$) 3D hills enhance σ_u (primarily between $-1 \lesssim x/L \lesssim 0$ and $-1 \lesssim y/L \lesssim 1$), enhance σ_v more broadly spatially across the hill, and slightly diminish σ_w (in a similar spatial region as σ_u). On the leeward side of the steep 3D hills: (i) σ_u rapidly diminishes to magnitudes below upstream values over a similar range of y/L ($-1 \lesssim y/L \lesssim 1$) but extending to at least $x/L = 6$; (ii) σ_v diminishes below upwind values over most of the hill's leeward region, but then picks up again when the terrain flattens; (iii) σ_w increases throughout the leeward hill region peaking at the hill base and then slowly returns to upstream values by approximately $x/L = 4$.

Steep 3D hills ($s_m = 0.26$) reduce the vertical flux of streamwise momentum at canopy-top across their entire windward side, with peak reductions down to as low as $\langle u'w' \rangle / u_*^2 \sim 0.1$ between $-1 \lesssim x/L \lesssim 0$ and $-1 \lesssim y/L \lesssim 1$, i.e. the region coincident with the largest positive hill-induced streamwise pressure gradient (figure 12e). Steep 3D hills ($s_m = 0.26$) accentuate $\langle u'w' \rangle / u_*^2$ at canopy-top primarily on the outward flanks

(between $0.5 \lesssim x/L \lesssim 2$ and $0.5 \lesssim \pm y/L \lesssim 1.5$). Vertical shear of the spanwise wind (figure 10) driven by the hill-induced pressure gradient ensures an importance of canopy-top vertical flux of spanwise momentum ($\langle v'w' \rangle/u_*^2$) on the outer flanks of the hill, with peaks between $-1 \lesssim x/L \lesssim 0$ and $0.5 \lesssim \pm y/L \lesssim 1.5$, however, the hill-induced peaks of $\langle v'w' \rangle/u_*^2$ are of notably smaller magnitude than the hill-induced modification to $\langle u'w' \rangle/u_*^2$. Flow divergence around the windward side of the hill produces a spanwise flux of streamwise momentum ($\langle u'v' \rangle/u_*^2$). More importantly, large-amplitude spanwise fluxes of streamwise momentum in the hill's lee participate strongly in laterally transporting streamwise momentum leaking around the hill-sides to regions inward behind hill-crest– a flow recovery mechanism not present in flow over 2D hills. The variability in figure 16 highlights limitations of the finite duration time-averaging in the 3D-hill cases.

7. Evaluating current theory

The small perturbation theory outlined in § 2 was originally developed for predicting turbulence over very low hills but is frequently applied outside its strict range of validity. The present LES data provide an opportunity to evaluate the analytic theory when applied to flows in Regime 4. Here, we evaluate how well results on the 2D ridges and on the plane of symmetry of the 3D hills follow the analytic theory.

7.1. *Perturbation analysis description*

7.1.1. *Turbulence production terms in streamline coordinates*

Current theory describing turbulent flow over forested hills hinges on equations written in streamline coordinates that simplify interpretation of the hill-induced forces perturbing the flow (e.g. Finnigan & Belcher 2004). The dominant production terms in the 2D Reynolds stress equations valid for the LES along hill-centreline in streamline coordinates can be written as

$$\tilde{u}\,\frac{\partial\,\langle \tilde{u}'\tilde{w}'\rangle}{\partial \tilde{x}} = -\,\sigma_{\tilde{w}}^2\,\frac{\partial \tilde{u}}{\partial \tilde{z}} - \frac{1}{2}\langle \tilde{u}'\tilde{w}'\rangle\frac{\partial \tilde{u}}{\partial \tilde{x}} - \left(2\sigma_{\tilde{u}}^2 - \sigma_{\tilde{w}}^2\right)\frac{\tilde{u}}{R} + \cdots, \qquad (7.1)$$

$$\tilde{u}\,\frac{\partial\,\sigma_{\tilde{u}}^2}{\partial \tilde{x}} = -2\,\sigma_{\tilde{u}}^2\,\frac{\partial \tilde{u}}{\partial \tilde{x}} - 2\,\langle \tilde{u}'\tilde{w}'\rangle\,\frac{\partial \tilde{u}}{\partial \tilde{z}} + 2\,\langle \tilde{u}'\tilde{w}'\rangle\,\frac{\tilde{u}}{R} + \cdots, \qquad (7.2)$$

$$\tilde{u}\,\frac{\partial\,\sigma_{\tilde{w}}^2}{\partial \tilde{x}} = \;\; 2\,\sigma_{\tilde{w}}^2\,\frac{\partial \tilde{u}}{\partial \tilde{x}} - 4\,\langle \tilde{u}'\tilde{w}'\rangle\,\frac{\tilde{u}}{R} + \cdots, \qquad (7.3)$$

where, the ellipses represent the triple moment, SGS, and canopy drag terms and the $\langle \rangle$ averaging notation is only retained for the covariances. Note that in (7.1) to (7.3) the sign convention applied to the streamline curvature $1/R$ is opposite to that used in Finnigan (1983) and Kaimal & Finnigan (1994). As in Finnigan (2024), we define R or $1/R$ as negative if the centre of curvature lies in the negative z direction (Aris 1990). In (7.1) to (7.3), the operators ($\partial/\partial \tilde{x}$, $\partial/\partial \tilde{z}$) denote directional derivatives parallel and perpendicular to the ($\tilde{x}$, $\tilde{z}$) coordinate lines, respectively. Velocity components ($\tilde{u}$, $\tilde{w}$) and turbulent stresses ($\sigma_{\tilde{u}}^2$, $\sigma_{\tilde{w}}^2$, $\langle \tilde{u}'\tilde{w}'\rangle$) in (7.1) to (7.3) should be interpreted as those that would be measured in a right-handed Cartesian coordinate frame ($\tilde{x}$, $\tilde{z}$) aligned at any point with its $\tilde{x}$-axis tangent to the streamline and its $\tilde{z}$-axis normal to the streamline. This coordinate system has the advantage that velocity vectors and tensors have their usual dimensions and interpretation but comes at the cost that partial derivatives must be replaced by directional derivatives (Finnigan 2024).

7.1.2. *Production terms in terrain-following coordinates*

Flow separation complicates the use of streamline coordinates. We therefore turn to a coordinate system tied with the terrain-following coordinate surfaces of the simulation which remain well-defined even in the presence of flow separation. Upwind of any flow separation, we expect that the terrain-following coordinate lines do not depart very far from streamlines.

As an approximation to flow variables transformed into streamline coordinates in (7.1) to (7.3), we transform the LES flow variables into a system defined relative to the local tangent of the coordinate surfaces, i.e. we approximate $\tilde{u}$ and $\tilde{w}$ as

$$\tilde{u} \approx \quad u\,e_1 + w\,e_3, \quad \text{and} \tag{7.4}$$

$$\tilde{w} \approx -u\,e_3 + w\,e_1. \tag{7.5}$$

where, $e_1 = \mathrm{d}x/(\mathrm{d}x^2 + \mathrm{d}z^2)^{(1/2)}$ and $e_3 = \mathrm{d}z/(\mathrm{d}x^2 + \mathrm{d}z^2)^{(1/2)}$.

Turbulence statistics of variables in this terrain-following coordinate system ($\langle \tilde{u}'\tilde{w}' \rangle$, $\sigma_{\tilde{u}}^2$, $\sigma_{\tilde{w}}^2$) are approximated by locally rotating time-averaged statistics of LES-derived variables calculated during the simulations into the terrain-following coordinate system via

$$\langle \tilde{u}'\tilde{w}' \rangle \approx -\sigma_u^2 e_1 e_3 + \langle u'w' \rangle (e_1^2 - e_3^2) + \sigma_w^2 e_1 e_3, \tag{7.6}$$

$$\sigma_{\tilde{u}}^2 \approx \sigma_u^2 e_1^2 + 2\langle u'w' \rangle e_1 e_3 + \sigma_w^2 e_3^2, \tag{7.7}$$

$$\sigma_{\tilde{w}}^2 \approx \sigma_u^2 e_3^2 - 2\langle u'w' \rangle e_1 e_3 + \sigma_w^2 e_1^2. \tag{7.8}$$

The directional derivatives ($\partial/\partial\tilde{x}$, $\partial/\partial\tilde{z}$) in (7.1) to (7.3) are approximated by derivatives along the LES coordinate surfaces (i.e. $\partial/\partial\tilde{x} \approx \partial/\partial\xi = \partial/\partial x$, and $\partial/\partial\tilde{z} \approx \partial/\partial\zeta$), where we have taken advantage of the fact that $\xi = x$ (and $\mathrm{d}\xi = \mathrm{d}x$) in our code. An incremental arclength along a terrain-following coordinate line $\mathrm{d}\tilde{x} \approx \mathrm{d}x(1 + s^2)^{(1/2)}$, where $s = \mathrm{d}z/\mathrm{d}x$ is the local slope of the coordinate line. We additionally assume $\mathrm{d}\tilde{x} \approx \mathrm{d}x$ and recognize that the maximum slope s_m of any terrain-following coordinate line in our simulations is 0.26 and that this choice introduces a small error in the derivatives of $\lesssim 3.3\,\%$.

7.1.3. *Analysis heights*

We investigate the relationship between the changes to the mean flow and the Reynolds stresses in three layers: (i) the upper canopy layer $h_c > z > d$ (where d is the canopy's displacement height, Appendix B); (ii) the inner shear stress layer $\widehat{h_i} > z > h_c$; (iii) the middle layer $\widehat{h_m} > z > \widehat{h_i}$. We therefore present variations of the mean flow and turbulence along lines of constant ζ midway through the middle layer at $\zeta_m = \widehat{h_i} + 0.5(\widehat{h_m} - \widehat{h_i})$, midway through the inner surface layer at $\zeta_i = h_c + 0.5(\widehat{h_i} - h_c)$ and in the upper canopy at $\zeta_c = 0.75h_c$. Since the middle layer and inner layer depths depend on the hill length scale L (see § 3 and Appendix B), ζ_i and ζ_m change with hill steepness. Upwind of any flow separation, the terrain-following coordinate lines, ζ_m, ζ_i, ζ_c do not depart too far from streamlines.

7.2. *Hill-induced flow perturbations*

7.2.1. *Middle layer*

Figure 17a shows for all four cases that increases in $\Delta\tilde{u}$ (where, $\Delta\tilde{u} = \langle \tilde{u} \rangle - u_b$, and $u_b = \langle \tilde{u} \rangle_b$) are nearly in phase with the hill crest as we expect given that the flow perturbations in the outer region are primarily an inviscid response to the pressure field induced by the hill. Consequently, the steeper hills produce larger $\Delta\tilde{u}$ than the shallower hills, and the 2D hills produce larger $\Delta\tilde{u}$ than the 3D hills. $\Delta\tilde{u}$ in the 3D-hill cases also takes more than $8L$ to recover to its upwind undisturbed value although comparison with figure 7 shows that
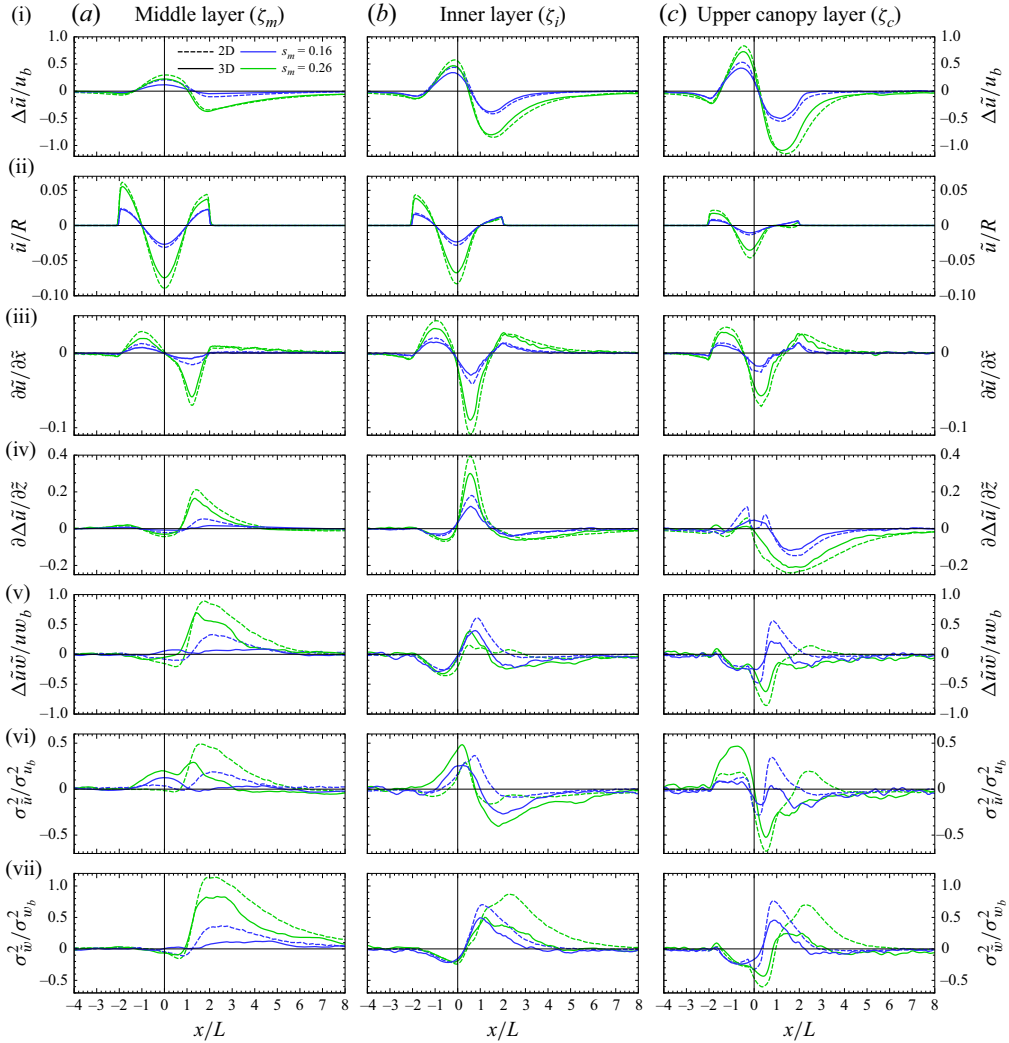
Figure 17. Streamwise variation of hill-induced perturbations of mean first- and second-order statistics relative to background values in the undisturbed flow upwind of the isolated hills (marked as $_b$) along the three constant ζ-coordinate surfaces: (*a*) middle-layer, ζ_m; (*b*) inner-layer, ζ_i; (*c*) upper canopy layer, ζ_c; see § 7.1.3 for the definition of ζ_m, ζ_i and ζ_c. Panels (i) present perturbation streamwise velocity ($\Delta\tilde{u}/u_b = (\langle\tilde{u}\rangle - u_b)/u_b$, where $u_b = \langle\tilde{u}\rangle_b$). Panels (ii) depict the variation of the centrifugal acceleration $\tilde{u}/R$ (in units of s^{-1}). Panels (iii) show $\partial\tilde{u}/\partial\tilde{x} = \partial\Delta\tilde{u}/\partial\tilde{x}$ (in units of s^{-1}). Panels (iv) present the perturbation vertical gradient of streamwise velocity $\partial\Delta\tilde{u}/\partial\tilde{z}$. Panels (v) present perturbation streamwise momentum stress ($\Delta\tilde{u}\tilde{w}/uw_b = (\langle\tilde{u}'\tilde{w}'\rangle - uw_b)/uw_b$, where $uw_b = \langle\tilde{u}'\tilde{w}'\rangle_b$). Panels (vi) present perturbation streamwise velocity variance ($\Delta\sigma_{\tilde{u}}^2/\sigma_{u_b}^2 = (\sigma_u^2 - \sigma_{u_b}^2)/\sigma_{u_b}^2$, where $\sigma_{u_b}^2 = \langle\tilde{u}'^2\rangle_b$), and panels (vii) present vertical velocity variance ($\Delta\sigma_{\tilde{w}}^2/\sigma_{w_b}^2 = (\sigma_{\tilde{w}}^2 - \sigma_{w_b}^2)/\sigma_{w_b}^2$, where $\sigma_{w_b}^2 = \langle\tilde{w}'^2\rangle_b$). Long-dashed lines present results for cases with isolated 2D hills, and solid lines present results for cases with 3D hills along hill-centreline; blue colours, $s_m = 0.16$; green colours, $s_m = 0.26$. A 1-2-1 smoothing in the streamwise direction has been applied to all fields. The mean wind flow is from left to right (in the $+x$ direction). See Appendix A for description of quantities marked with $_b$.

ζ_m is above the separation bubble. The vertical gradient of mean perturbation streamwise velocity $\partial\Delta\tilde{u}/\partial\tilde{z}$ decreases at this height starting at $x/L \sim -1$ for all cases, and then becomes positive at approximately $x/L \sim 1$ with notably larger increased vertical shear in the cases with steeper hills ($\sim 35\%$ increase for cases with $s_m = 0.16$ versus $\sim 180\%$

increase for cases with $s_m = 0.26$). The streamwise velocity gradient, $\partial \tilde{u}/\partial \tilde{x}$ ($= \partial \Delta \tilde{u}/\partial \tilde{x}$) peaks on the upwind slope and attains its lowest values on the lee slope with the largest values on the 2D ridges.

The third important mean strain term appearing in the production terms of the Reynolds stress (7.1) to (7.3) is $\tilde{u}/R$, where R is the local radius of curvature of the surface-following coordinate lines. The effects of rotation on the turbulent stresses are particularly important and are often expressed in terms of a curvature Richardson Number Ri_c because the centrifugal forces generated following a curved trajectory are analogous to the effects of buoyancy but have a larger effect on the turbulence than a simple comparison of $\tilde{u}/R$ with other strains such as $\partial \tilde{u}/\partial \tilde{x}$ or $\partial \Delta \tilde{u}/\partial \tilde{z}$ would suggest (Bradshaw 1969, 1973; Finnigan 1983). Here $\tilde{u}/R$ attains its largest positive values over the upwind and downwind concave hill surfaces and its largest negative values over the convex hill crest. The combination of greater curvature and larger velocity perturbations on the steeper ($s_m = 0.26$) hills implies $\tilde{u}/R$ is more than twice as large on those hills as on the shallower ($s_m = 0.16$) hills.

Streamwise velocity variance $\sigma_{\tilde{u}}^2$ increases up to the hill crest on the 3D hills but decreases slightly on the 2D hills; this likely represents a response to the greater streamwise acceleration over the 2D ridges as the first production term in (7.2), $[-2\,\sigma_{\tilde{u}}^2\,(\partial \tilde{u}/\partial \tilde{x})]$ represents stretching of vortex tubes aligned in the streamwise direction, which increases $\sigma_{\tilde{v}}^2$ and $\sigma_{\tilde{w}}^2$ at the expense of $\sigma_{\tilde{u}}^2$. The slight decrease in shear, $\partial \Delta \tilde{u}/\partial \tilde{z}$ and in $\Delta \tilde{u}\tilde{w}$, adds to the decrease in $\sigma_{\tilde{u}}^2$ production but the third production term $2\,\langle \tilde{u}'\tilde{w}'\rangle\,(\tilde{u}/R)]$ acts to augment $\sigma_{\tilde{u}}^2$ over the 3D hills as both $\langle \tilde{u}'\tilde{w}'\rangle$ and $\tilde{u}/R$ are negative. The most prominent feature of the $\sigma_{\tilde{u}}^2$ evolution is the large increase on the lee slope over the 2D hills and the steeper 3D hill. This large increase is likely associated with the large increase in mean shear $\partial \Delta \tilde{u}/\partial \tilde{z}$ bounding the upper edge of the separation bubble. This finding is not evident over the shallower 3D hill where there is no increase in $\sigma_{\tilde{u}}^2$.

7.2.2. *Inner layer*

In the inner layer (figure 17b), $\Delta \tilde{u}$ initially decreases with approach to the hill, then at $x/L \sim -1$, $\Delta \tilde{u}$ increases to maximum values occurring just upwind of hill-crest ($x/L = 0$), and then diminishes to a minima at $x/L \sim 1.5$. The breaking of the symmetry between $\Delta \tilde{u}$ and the hill profile seen in the middle layer, results from the action of hill-induced perturbations on the shear stress $\langle \tilde{u}'\tilde{w}'\rangle$. This asymmetry leads in turn to generation of aerodynamic drag on the hill. The maxima and minima in $\Delta \tilde{u}$ are $\sim 10\,\%$ higher for the cases with 2D hills compared with 3D hills and shift slightly upwind for cases with $s_m = 0.26$. At this height, flow over hills of $s_m = 0.16$ recovers its upwind $\Delta \tilde{u}$ value by $x/L \sim 6$, while flow over hills with $s_m = 0.26$ recover their upwind values by $x/L \sim 8$.

Compared with the middle layer, hill-induced variations in $\partial \Delta \tilde{u}/\partial \tilde{z}$ shift upwind by $x/L \sim 0.5$ with a minimum just upwind of hill-crest (i.e. at $x/L \sim -0.5$), a maximum downwind of hill-crest (i.e. at $x/L \sim 0.5$), which is much larger on the steeper hills and is probably associated with the strong shear capping the separation bubble. A downwind minimum occurs at $x/L \sim 3$ from which all cases do not recover their upwind values until $x/L \sim 8$.

Variations in $\sigma_{\tilde{u}}^2$ on the 2D hills in the inner layer are largely in phase with $\partial \Delta \tilde{u}/\partial \tilde{z}$, which is the dominant mean strain entering the largest production term, $[-2\,\langle \tilde{u}'\tilde{w}'\rangle\,(\partial \tilde{u}/\partial \tilde{z})]$ in (7.2). This response in $\sigma_{\tilde{u}}^2$ is amplified by the reduction in $\Delta \tilde{u}\tilde{w}$, a reduction itself largely driven by the changes in $\partial \Delta \tilde{u}/\partial \tilde{z}$ as we can see from (7.3) as well as by the damping effect of streamline curvature over the convex hill slope before flow separation occurs. Over the 3D hills, we see an increase in $\sigma_{\tilde{u}}^2$ on the upwind slope, which could be attributed to the unstable curvature upwind of $x/L \sim -1$.

The reduction in $\sigma_{\tilde{w}}^2$ over the hill crest can be associated with the reduction in the vortex stretching strain $\partial \tilde{u}/\partial \tilde{x}$ just ahead of the hill but is primarily attributable to the effect of the curvature term $[-4\langle \tilde{u}'\tilde{w}'\rangle (\tilde{u}/R)]$, which acts to reduce $\sigma_{\tilde{w}}^2$ directly. However, stabilizing curvature also reduces $\langle \tilde{u}'\tilde{w}'\rangle$ over the hill crest and this change also feeds through to slightly mitigate curvature's damping effect on $\sigma_{\tilde{w}}^2$. Changes in $\langle \tilde{u}'\tilde{w}'\rangle$ closely follow the changes in $\partial \Delta \tilde{u}/\partial \tilde{z}$ until the separation bubble and wake is encountered at $x/L \sim 1$. The large spike in $\langle \tilde{u}'\tilde{w}'\rangle$ at $x/L \sim 1$ is likely associated with the free shear layer at the upper boundary of the bubble. Here $\langle \tilde{u}'\tilde{w}'\rangle$ is also strongly reduced by curvature's damping effect over the crest through the third, curvature-linked, production term in (7.1). The largest impact of separation is on $\sigma_{\tilde{w}}^2$ behind the steepest 2D ridge and this is where we would expect the most active and established separation region (figure 14) although we see large increases in $\sigma_{\tilde{w}}^2$ on the other hills also. Somewhat surprisingly, $\sigma_{\tilde{u}}^2$ reduces behind the hill with the largest reduction occurring behind the 3D hills.

7.2.3. *Upper canopy layer*

The first striking difference between the inner layer and the upper canopy layer is the upwind shift in the positive peak in $\Delta \tilde{u}$ which now occurs at $x/L \sim -0.5$. The negative peak in $\Delta \tilde{u}$ upwind of the hill also moves farther upwind and both peaks increase in magnitude. Finnigan & Belcher (2004) explain these upwind movements of the $\Delta \tilde{u}$ peaks as a physical consequence that in the lower canopy, the background velocity u_b becomes smaller than the velocity perturbations, which are driven by the hill-induced pressure perturbations that are able to pass through the canopy unimpeded. Consequently, the $\Delta \tilde{u}$ perturbations come into phase with the pressure gradient $-\partial \langle p \rangle/\partial x$ which has its maximum positive value around $x/L \sim -2$ (figure 13). The upper and lower canopy velocity fields are connected by turbulent mixing so the upper canopy $\Delta \tilde{u}$ perturbation is dragged upwind compared with $\Delta \tilde{u}$ in the inner layer. The Finnigan & Belcher (2004) theory (applicable in Regime 1, figure 4) assumes that the velocity shear $\partial \tilde{u}/\partial \tilde{z}$ and shear stress $\langle \tilde{u}'\tilde{w}'\rangle$ in the lower canopy are both negligible so that the velocity perturbations are driven only by $-\partial \langle p \rangle/\partial x$, not by turbulent momentum transfer. Figures 8 and 15 show that in the present 'shallow canopy' (Regime 4) configuration, velocity shear in the lower canopy is significant and $\langle \tilde{u}'\tilde{w}'\rangle$ cannot be ignored. We therefore expect that the velocity perturbations in the lower canopy are less closely linked to the pressure gradient but also share some of the dynamics of the upper canopy flow where velocity perturbations more closely follow the pressure perturbations. Consequently we expect that the upwind shift of the velocity peak observed here is smaller than would be observed over the same hill contour covered by a denser and/or deeper canopy.

The strongly negative $\Delta \tilde{u}$ perturbations in the lee of the hill indicate separation within the canopy on both steeper and shallower hills. Recall that the Finnigan & Belcher (2004) theory predicts that separation can occur within the canopy even on hills which are too shallow for the separation bubble to extend into the inner and middle layers. The strain fields, $\tilde{u}/R$, $\partial \tilde{u}/\partial \tilde{x}$ and $\partial \Delta \tilde{u}/\partial \tilde{z}$ also change in the upper canopy. While $\tilde{u}/R$ and $\partial \tilde{u}/\partial \tilde{x}$ closely follow the pattern of the inner layer with their variations simply being reduced in magnitude, $\partial \Delta \tilde{u}/\partial \tilde{z}$ departs distinctly from its inner layer behaviour. The four hills each generate different and complicated $\partial \Delta \tilde{u}/\partial \tilde{z}$ evolution upwind and around the hilltop, with the $s_m = 0.16$ and more strikingly the $s_m = 0.26$ hills exhibiting strong reductions in vertical shear with minima at $x/L \sim 2$. These presumably signal the presence of within-canopy separation.

The evolution of $\sigma_{\tilde{u}}^2$ in the upper canopy is difficult to explain simply in terms of the production terms in (7.1) to (7.3). In all four simulations, $\sigma_{\tilde{u}}^2$ increases upwind of the hill

crest. The largest production term in (7.2) is $[-2\langle \tilde{u}'\tilde{w}'\rangle (\partial \tilde{u}/\partial \tilde{z})]$ but $\langle \tilde{u}'\tilde{w}'\rangle$ falls where $\sigma_{\tilde{u}}^2$ increases while changes in $\partial \Delta\tilde{u}/\partial\tilde{z}$ are small. The vortex stretching strain $\partial\tilde{u}/\partial\tilde{x}$ is large on the upwind slope for both the steeper 2D and 3D hills and this term should act to reduce $\sigma_{\tilde{u}}^2$ and increase $\sigma_{\tilde{w}}^2$ but instead the latter decreases on the upwind slope. This decrease in $\sigma_{\tilde{w}}^2$ can be explained by the damping effect of streamline curvature which is apparently larger than production by vortex stretching. The fluctuating canopy-drag covariance term $\langle \tilde{u}'\tilde{F}_x'\rangle$ (not shown) acts as a sink of variance on the windward side of the hill and a weak source in the hill lee but is of insufficient amplitude to overwhelm the production terms. There is a positive contribution to $\sigma_{\tilde{u}}^2$ from the curvature term $2\langle \tilde{u}'\tilde{w}'\rangle (\tilde{u}/R)$ but it is difficult to understand why this should have a large positive effect on the isolated steep hill but not the steep 2D hill.

We tentatively conclude that the redistribution of energy between $\sigma_{\tilde{u}}^2$ and $\sigma_{\tilde{w}}^2$ in the canopy by pressure and its interaction with the lower boundary (possibly because these simulations lie within Regime 4) prevents interpretation of the upper canopy Reynolds stresses in terms of the mean flow straining alone. Here $\sigma_{\tilde{u}}^2$, $\sigma_{\tilde{w}}^2$ and $\langle \tilde{u}'\tilde{w}'\rangle$ all show large peaks behind the hill on both the steeper and shallower hills, with the peaks on the shallower 2D and 3D hills occurring around $x/L \sim 2$ whereas on the steeper hills the peaks are displaced downwind to $x/L \sim 3$ and preceded by a dip just behind the crest, which presumably corresponds to separated flow.

8. Summary and conclusions

To advance understanding of the hill-slope's and hill-shape's role on turbulent air flow over isolated forested hills, we interrogate four turbulence-resolving simulations. A spectrally friendly fringe-technique enables the use of periodic boundary conditions to simulate flow over isolated 2D and 3D hills of cosine shape. The simulations target recently conducted WT experiments that are configured to fall outside the regimes for which current theory applies.

First, simulation skill for flow over isolated 3D hills is demonstrated through matching the canopy and hill configuration with the recently conducted WT experiments and intercomparing results. Subsequently, response of the mean and turbulent flow components to 2D versus 3D hills along hill-centreline are discussed. Finally, a discussion of the phase and amplitude of spatially varying responses of flow over forested hills are evaluated. Our analysis provides insight into flow features induced by changes in hill shape and slope when in Regime 4, and to the mechanisms behind and locations where assumptions made when developing current theory fail towards advancing theory to regimes beyond Regime 1.

Key findings include the following.

(i) Flow over isolated 2D forested hills produces larger amplitude vertical motions on a hill's windward and leeward faces and speed-up of the mean wind compared with that over isolated 3D forested hills at hill-centreline. At canopy top, maximum speed up $\max(\Delta u/u_b)_{h_c}$ occurs at approximately $x/L = -0.3$. A change in hill slope from $s_m = 0.16$ to 0.26 increases $\max(\Delta u/u_b)_{h_c}$ by approximately 30 % for 2D hills and 34 % for 3D hills. Flow separation induced by the steeper $s_m = 0.26$ hills ensures that mean flow fields require notably longer distances downstream of the hill before full recovery (i.e. not until $6 \lesssim x/L \lesssim 8$).

(ii) 3D hills generate surface pressure minima over hill-crest that are nearly half the magnitude of those over 2D hills. The 3D hills influence the pressure field in the

spanwise direction out to $y/L \sim \pm 3$. Pressure gradients in the spanwise direction are smaller than in the streamwise direction, but the spanwise pressure gradients are of sufficient amplitude to overcome downward turbulent momentum transport into the canopy and drive mean uphill within-canopy flow on the hill flanks. The spatial region over which the hill-induced negative pressure drag acts increases with increasing hill steepness, however, the horizontal extent over which this thrust force acts decreases as the hills change from a 2D ridge to an axisymmetric 3D hill.

(iii) The perturbation analysis in § 7 suggests that the assumptions about the dominant flow dynamics embodied in partitioning the flow into an upper layer with an inviscid response to the hill's pressure field, an inner layer where changes to the shear stress and the mean flow are strongly coupled and a canopy layer where the nonlinear treatment of velocity perturbations in the lower canopy affects flow throughout the layer are robust inasmuch as they lead to solid predictions of hill-induced perturbations to the mean flow. However, when we try to apply those assumptions to predict the evolution of the turbulent moments, we find they provide approximate explanations at best. This is especially true in the upper canopy, where additional canopy-induced physics affects the transfer of TKE between orthogonal velocity components.

The results presented only scratch at the surface of understanding how hill shape and steepness modulate turbulent flow over low hills covered with a shallow forest canopy (Regime 4 in the L/L_c versus h_c/L_c parameter space) and how well current theory predicts their interaction. In particular, this analysis focuses on neutrally stratified conditions; inclusion of buoyancy forces would likely alter the current findings substantially.

Declaration of interests. The authors report no conflict of interest.

Author contributions. E.G.P. designed, implemented, ran and analysed the numerical simulations. I.N.H. designed, implemented, conducted and analysed the WT experiments. J.J.F. helped design the WT experiments and interpret the results. P.P.S. developed the backbone of the LES code and helped interpret the results. E.G.P. wrote the initial draft of the manuscript; J.J.F., I.N.H. and P.P.S. provided feedback and helped rewrite aspects of the manuscript.

Data availability statement. Upon journal acceptance, the processed data used to produce the figures contained within this manuscript will be made available on NCAR's Geoscientific Data Exchange (GDEX).

Appendix A. Assessing background inflow conditions

Section 5 compares time-averaged profiles at a single location. Harman *et al.* (2016) demonstrated that a single profile in the vicinity of a single canopy element does not accurately represent the horizontal average due to variability of the time-mean with position relative to the canopy element. To ascertain the potential spatial variability of the observations collected over the 3D hills, Harman & Finnigan (2018) performed a

detailed spatial sampling experiment upstream of the hills collecting profiles at 16 different spatial locations surrounding a single peg – similar to that Harman *et al.* (2016) conducted around their tombstone elements. The LES does not physically resolve individual canopy elements, hence the wind fields averaged over these 16 different profiles should better represent the LES predictions than would any individual observed profile. Therefore, to more completely assess the numerical and physical inflow conditions approaching the hills, figure 18 presents a comparison of the detailed spatial sampling WT measurements and the LES, where the LES results reflect time-averaged flow fields that have been horizontally averaged over the entire upwind fringe region. The horizontal bars on the WT data reflect $\pm$ one standard deviation of each statistic associated with the 16 time-averaged profiles.

Normalized mean wind fields in the approach flow compare well between the WT and the LES and generally with expectation. Mean streamwise velocity is approximately logarithmic with increasing height above the canopy and decays exponentially with descent within. Spanwise and vertical velocity nearly vanish in the absence of a Coriolis force and as a result of zero flow through the underlying surface. However, in the WT, vertical velocity remains finite above the canopy resulting primarily from a combination of slight errors in the matrix used to rotate from laser coordinates to Cartesian coordinates, but Harman & Finnigan (2018) also speculate that the finite downward mean velocity observed in the WT might reflect a small bias in the seed fog resulting from its continual deposition to the underlying canopy element surface. The substantial variability of the within-canopy spanwise and vertical velocity observations about the 16 profiles is also notable.

Second-order moments in the LES adhere nicely to expectation (e.g. Raupach *et al.* 1996), and only differ slightly from the WT observations. Momentum flux above the canopy is nearly constant with height; where compared with the zero-pressure gradient WT, having imposed a finite pressure gradient in the LES ensures that $\langle u'w'\rangle_b/u_*^2$ falls off linearly with height between canopy-top and the top of the domain such that the minimal reduction of $\langle u'w'\rangle_b/u_*^2$ between $z/h_c = 1$ and 3 in the LES speaks to the fact that the domain is over 133 times taller than the canopy. Consistent with Harman *et al.* (2016), $\langle u'w'\rangle_b/u_*^2$ in the WT shows a peak at canopy top thought to result from insufficient sampling of flow in proximity to the canopy elements. Momentum absorption through pressure drag induced by the canopy ensures that $\langle u'w'\rangle_b/u_*^2$ diminishes nearly exponentially with descent into the canopy for both the WT and LES. Somewhat counter to expectation (e.g. $\langle v'w'\rangle_b/u_*^2 = 0$) is that $\langle v'w'\rangle_b/u_*^2$ exhibits a small increase with increasing height in the WT. Velocity standard deviations $(\sigma_{u_b}, \sigma_{v_b}, \sigma_{w_b})/u_*$ also generally agree well with each other and expectation, but diminish with decreasing height from canopy top more rapidly in the LES than in the WT – a result that could again suggest that as many as 16 observed profiles may still not reflect the total flow field variability.

Profiles of velocity skewness from the LES are consistent with most outdoor field observations (i.e. positive streamwise velocity skewness Sk_{u_b} and negative vertical velocity skewness Sk_{w_b} at canopy top, which reflect the organized nature of the turbulence at canopy top thought to be produced by an inflection point instability of the mean wind profile (e.g. Raupach *et al.* 1996; Finnigan *et al.* 2009). Here Sk_{w_b} in the WT is negative within the canopy, but is positive at canopy top and above; such Sk_{w_b} profiles have been observed previously, but primarily in wind and water tunnel flows sampling in the vicinity of sparse organized canopy element structure (e.g. the tombstone, rods and light-bulb elements discussed in Raupach *et al.* (1996), Poggi *et al.* (2004) and Böhm *et al.* (2013) suggesting that the flow sampled in the WT might be reflective of a wall-bounded shear flow with canopy drag augmented by wakes shed in the element lee. Nevertheless,
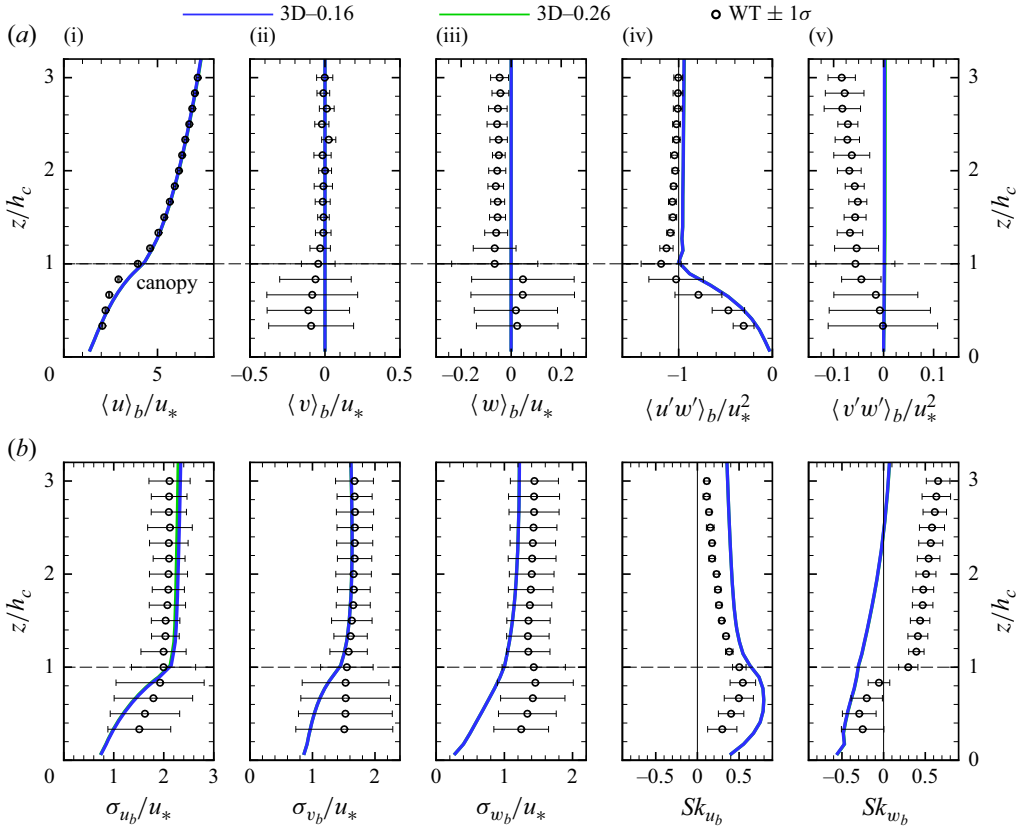
Figure 18. An intercomparison of WT profile statistics spatially averaged over 16 individual profiles that spatially sample the within-canopy airspace surrounding a single canopy element and its neighbours, compared with profile statistics derived from the LESs which have been horizontally averaged over the entire upwind fringe region; these profiles represent the background inflow conditions (labelled as $_b$). From (i) to (v), panels (a) depict mean streamwise velocity $\langle u \rangle_b$, spanwise velocity $\langle v \rangle_b$, vertical velocity $\langle w \rangle_b$, vertical flux of streamwise momentum $\langle u'w' \rangle_b$ and the vertical flux of spanwise momentum $\langle v'w' \rangle_b$, and panels (b) present profiles of streamwise velocity standard deviation $\sigma_{u_b} = \langle u'^2 \rangle_b^{1/2}$, spanwise velocity standard deviation $\sigma_{v_b} = \langle v'^2 \rangle_b^{1/2}$, vertical velocity standard deviation $\sigma_{w_b} = \langle w'^2 \rangle_b^{1/2}$, streamwise velocity skewness $Sk_{u_b} = \langle u'^3 \rangle_b / \sigma_{u_b}^3$ and vertical velocity skewness $Sk_{w_b} = \langle w'^3 \rangle_b / \sigma_{w_b}^3$. Where noted, quantities are normalized by the friction velocity u_* (or u_*^2) to ensure proper comparison. Solid lines depict the LES results and symbols the WT results along with horizontal bars marking $\pm$ one standard deviation associated with the 16 independently observed profiles comprising the mean. Results from 3D–0.16 are in blue, and from 3D–0.26 are in green (the green lines were drawn first, so they are hidden beneath the blue lines).

the results presented in figure 18 clearly demonstrate the comparability of the WT and LES inflow conditions impinging on the hills and provide a measure of the variability anticipated by sampling a single profile over the forested WT hills.

Appendix B. Defining the inner shear stress layer and middle layer depths

Small perturbation analyses of turbulent flow over low hills (Jackson & Hunt 1975; Hunt *et al.* 1988; Belcher *et al.* 1993) divide the flow into separate layers with different physical processes dominating the flow in each layer. Separate solutions to the flow equations are found for each layer and the resulting integration constants are determined by asymptotic

matching between the layers. Two main regions are defined, the outer, where the response to the pressure field generated by flow over the hill is inviscid, and the inner, where perturbations to the turbulent Reynolds stresses affect the perturbations to the mean flow. Each region is further divided into layers. The middle layer of depth h_m is the lower part of the outer region and in this region the flow responses are inviscid but rotational to accommodate shear in the approach flow. In the upper layer, which extends from h_m to the top of the boundary layer, flow responses are irrotational and can be computed by potential theory. The inner region consists of the shear stress layer of depth h_i, and the thin inner surface layer, of depth l_s, which allows formal matching with the surface boundary condition. In the inner region, perturbations to the turbulent stresses affect the perturbations to the mean flow.

Hunt *et al.* (1988) and Belcher *et al.* (1993) define the middle layer depth by an implicit formula

$$\frac{h_m}{L} \ln^{1/2}\left(\frac{h_m}{z_\circ}\right) \sim 1, \tag{B1}$$

where $z_\circ$ is the roughness length of the surface and L the half-length or horizontal length scale of the hill. If $\ln(L/z_\circ) \gg 1$, (B1) can be approximated by an explicit relationship,

$$\frac{h_m}{L} \ln^{1/2}\left(\frac{L}{z_\circ}\right) \sim 1. \tag{B2}$$

The shear stress layer depth h_i is also defined by an implicit relationship,

$$\frac{h_i}{L} \ln\left(\frac{h_i}{z_\circ}\right) = 2\kappa^2. \tag{B3}$$

Where κ is von Kármán's constant. Hunt *et al.* (1988) give two different ways of deriving this definition while Belcher *et al.* (1993) arrive at the same formula by a slightly different route.

Most variation of the shear stress perturbation with height occurs through h_i above the inner surface layer of depth $l_s \ll h_i$. However, across l_s, the shear stress gradient $\partial \langle u'w' \rangle / \partial z$ changes rapidly to match the surface streamwise pressure gradient at $z = z_\circ$. The depths of the middle layer h_m (B2) and the shear stress layer h_i (B3) are derived formally in Hunt *et al.* (1988) and Belcher *et al.* (1993) based on several assumptions. First, that the 'background' velocity profile in the flow approaching the hill is assumed to be in equilibrium with the upstream surface and so can be described by the standard logarithmic law, *viz.*

$$u_b(z) = \frac{u_*}{\kappa} \ln\left(\frac{z}{z_\circ}\right) \tag{B4}$$

where u_* is the friction velocity. Second, that in the shear stress layer the hill-induced perturbations to the turbulent shear stress Δuw and to the mean velocity gradient $\partial \Delta u / \partial z$ obey the same mixing length relationship as in the logarithmic approach flow (B4), and third, that all the streamwise momentum is absorbed as drag or surface friction on the ground (at $z = z_\circ$).

However, (B3) can yield physically implausible results for h_i over surfaces covered with tall roughness, h_i from (B3) can be found at heights lower than the height of the roughness elements (Finnigan *et al.* 1990). This is particularly problematic over hills covered with tall canopies (e.g. Finnigan & Brunet 1995) or in the present experiment. Finnigan & Belcher (2004) extended the Hunt *et al.* (1988) model structure by replacing the thin inner surface layer l_s by a deep plant canopy parameterized by linearized flow equations in the upper

canopy but where the unavoidably nonlinear dynamics in the lower canopy were treated heuristically.

Identifying the inner shear stress layer depth (h_i) and the middle layer depth (h_m) is critical to applying the asymptotic small perturbation theory to interpret measurements or model results and so the definitions in (B1) and (B3) must be modified to account for the presence of a deep canopy. The first and most obvious change is that, if (B4) is used to describe the approach flow above the canopy, the origin of the z coordinate must be shifted from $z = 0$ to $z = d + z_\circ$, where d is the displacement height (or mean height of the within-canopy momentum sink, e.g. Kaimal & Finnigan (1994)) and $z_\circ$ now refers to the roughness length of the canopy, so that (B4) becomes

$$u_b(z) = \frac{u_*}{\kappa} \ln\left(\frac{z - d}{z_\circ}\right), \tag{B5}$$

so that $u_b(d + z_\circ) = 0$. The second set of changes follows from the fact that the flux-gradient relationship between turbulent shear stress and velocity shear in the RSL just above a tall canopy is altered by the presence of energetic coherent turbulence, which originates from the hydrodynamic instability of the inflection in the mean velocity profile, which always develops at the top of the canopy because of the distributed pressure drag on the foliage (Raupach 1994; Finnigan *et al.* 2009).

Harman & Finnigan (2007, 2008) have successfully parameterized this effect using RSL functions, $\widehat{\phi}((z - d)/\delta_\omega)$ and $\widehat{\psi}((z - d)/\delta_\omega)$, where δ_ω is the vorticity thickness evaluated at canopy top h_c. These RSL functions are analogous to the familiar Monin–Obukhov functions $\phi((z - d)/L_{MO})$ and $\psi((z - d)/L_{MO})$, which are used to accommodate diabatic stability in surface layer parameterizations, L_{MO} being the Obukhov length (e.g. Garratt 1992). After incorporating these RSL functions, the mixing length relationship and the above-canopy log law in the approach flow become, respectively,

$$\tau_b = u_*^2 = \kappa \, u_* \, (z - d) \, \widehat{\phi}^{-1}\left(\frac{z - d}{\delta_\omega}\right) \frac{\partial u_b}{\partial z}, \tag{B6}$$

and

$$u_b(z) = \frac{u_*}{\kappa}\left[\ln\left(\frac{z - d}{z_\circ}\right) + \widehat{\psi}\left(\frac{z - d}{\delta_\omega}\right)\right] \tag{B7}$$

where

$$\widehat{\psi}\left(\frac{z - d}{\delta_\omega}\right) = \int_{z-d}^{\infty} \frac{1 - \widehat{\phi}\left(\frac{z'}{l/\beta}\right)}{z'} \mathrm{d}z' \tag{B8}$$

is the integrated form of $\widehat{\phi}((z - d)/\delta_\omega)$. Harman & Finnigan (2007) define $\widehat{\phi}((z - d)/\delta_\omega)$ as

$$\widehat{\phi} = 1 - c_1 \exp\left(-\frac{\beta \, c_2 \, z}{l}\right), \tag{B9}$$

where $\beta = u_*/u_b$ evaluated at h_c, $L_c = (c_d \, a)^{-1}$, $l = 2 \, \beta^3 \, L_c$ and $c_1 = 1 - \widehat{\phi}(0)$. Here L_c is the momentum absorption length of the canopy, with c_d a leaf level drag coefficient and a the leaf area per unit volume of the foliage. In (B9), c_1 is a constant of integration and c_2 relates the vertical scale of the RSL to the vorticity thickness δ_ω. Following Harman & Finnigan (2008) we choose $c_2 = 1/2$, therefore (B9) yields $c_1 = e^{1/4}$. $\widehat{\psi}$ is obtained

1026 A16-35

from (B9). For example when $\widehat{\phi} = 1$,

$$\widehat{\psi} = c_1\, \Gamma \left(0,\, \frac{z}{8\, L_c^2\, \beta^6} \right), \tag{B10}$$

where Γ is the incomplete Gamma function.

The forms of the $\widehat{\phi}$ and $\widehat{\psi}$ functions as well as the examples of the application of this RSL theory to forest canopies of different form and density in Harman & Finnigan (2007, 2008) reveal that the presence of the $\widehat{\phi}$ function in the flux-gradient relationship (B6) reduces the mean velocity gradient $\partial u_b/\partial z$ in the RSL because the additional turbulent mixing produced by the coherent eddies produced by the canopy-induced inflection point instability (Raupach *et al.* 1996; Finnigan *et al.* 2009) allows the constant momentum flux $\tau_b = u_*^2$ to be supported by a smaller velocity gradient, while at the same time the actual velocity u_b in the RSL is increased by the $\widehat{\psi}$ term in (B7).

These changes to both the log law and to the flux-gradient relationship are incorporated in the following modified form of the implicit relationship for $\widehat{h_i}$ which is appropriate for use over a canopy or other tall roughness:

$$\frac{\widehat{h_i}}{L}\, \left[\ln \left(\frac{\widehat{h_i}}{z_\circ} \right) + \widehat{\psi}\, \left(\widehat{h_i} \right) \right] \widehat{\phi}\, \left(\widehat{h_i} \right) = 2\kappa^2. \tag{B11}$$

Equation (B11) yields the depth of the inner shear stress layer but the origin of the vertical coordinate is now the displacement height d and the location of the top of the shear stress layer must be measured from that location.

Equivalent adjustments to the formulae for h_m (B1) and (B2) should also be made. However, because the changes to u_b and $\partial u_b/\partial z$ are only significant within the RSL (which occupies only the lowermost portion of the shear stress layer), the only sensible change to h_m results from the upward shift in the origin of the vertical coordinate of $\widehat{h_m}$ to $z = d + z_\circ$.

REFERENCES

ARIS, R. 1990 *Vectors, Tensors, and the Basic Equations of Fluid Mechanics. Dover Books on Mathematics*. Dover Publications.

ARYA, S.P.S. & GADIYARAM, P.S. 1986 An experimental study of flow and dispersion in the wakes of three-dimensional low hills. *Atmos. Environ.* **20** (4), 729–740.

ATHANASSIADOU, M. & CASTRO, I.P. 2001 Neutral flow over a series of rough hills: a laboratory experiment. *Boundary-Layer Meteorol.* **101** (1), 1–30.

AYOTTE, K.W., FINNIGAN, J.J. & RAUPACH, M.R. 1999 A second-order closure for neutrally stratified vegetative canopy flows. *Boundary-Layer Meteorol.* **90** (2), 189–216.

AYOTTE, K.W. & HUGHES, D.E. 2004 Observations of boundary-layer wind-tunnel flow over isolated ridges of varying steepness and roughness. *Boundary-Layer Meteorol.* **112** (3), 525–556.

BELCHER, S.E., HARMAN, I.N. & FINNIGAN, J.J. 2011 The wind in the willows: flows in forest canopies in complex terrain. *Annu. Rev. Fluid Mech.* **44** (1), 479–504.

BELCHER, S.E., NEWLEY, T.M. & HUNT, J.C.R. 1993 The drag on an undulating surface induced by the turbulent boundary layer. *J. Fluid Mech.* **249**, 557–596.

BÖHM, M., FINNIGAN, J.J., RAUPACH, M.R. & HUGHES, D. 2013 Turbulence structure within and above a canopy of bluff elements. *Boundary-Layer Meteorol.* **146** (3), 393–419.

BOUGEAULT, P., BINDER, P., BUZZI, A., DIRKS, R., KUETTNER, J., HOUZE, R., SMITH, R.B., STEINACKER, R. & VOLKERT, H. 2001 The MAP special observing period. *Bull. Am. Meteorol. Soc.* **82** (3), 433–462.

BRADSHAW, P. 1969 The analogy between streamline curvature and buoyancy in turbulent shear flow. *J. Fluid Mech.* **36** (1), 177–191.

BRADSHAW, P. 1973 Effects of streamline curvature on turbulent flow. *Tech. Rep.* AG-169. North Atlantic Treaty Organization, Paris, France.

BRITTER, R.E., HUNT, J.C.R. & RICHARDS, K.J. 1981 Air flow over a two-dimensional hill: studies of velocity speed-up, roughness effects and turbulence. *Q. J. R. Meteorol. Soc.* **107** (451), 91–110.

CALERO, J.S. 2018 *Jean Le Rond D'Alembert: A New Theory of the Resistance of Fluids, Studies in History and Philosophy of Science*, vol. 47. Springer International Publishing.

CAWOOD, P.A., CHOWDHURY, P., MULDER, J.A., HAWKESWORTH, C.J., CAPITANIO, F.A., GUNAWARDANA, P.M. & NEBEL, O. 2022 Secular evolution of continents and the Earth system. *Rev. Geophys.* **60** (4), e2022RG000789.

CHAMECKI, M., FREIRE, L.S., DIAS, N.L., CHEN, B., DIAS-JUNIOR, C.Q., TOLEDO MACHADO, L.A., SÖRGEL, M., TSOKANKUNKU, A. & DE ARAÚJO, A.C. 2020 Effects of vegetation and topography on the boundary layer structure above the Amazon forest. *J. Atmos. Sci.* **77** (8), 2941–2957.

CHEN, B. & CHAMECKI, M. 2023 Turbulent kinetic energy budgets over gentle topography covered by forests. *J. Atmos. Sci.* **80** (1), 91–109.

CHEN, B., CHAMECKI, M. & KATUL, G.G. 2020 Effects of gentle topography on forest-atmosphere gas exchanges and implications for eddy-covariance measurements. *J. Geophys. Res.: Atmos.* **125** (11), e2020JD032581.

COMPUTATIONAL AND INFORMATION SYSTEMS LABORATORY. 2019 Cheyenne: HPE/SGI ICE XA System (NCAR Community Computing). Available at: https://doi.org/10.5065/D6RX99HX.

COMPUTATIONAL AND INFORMATION SYSTEMS LABORATORY. 2023 Derecho: HPE Cray EX System (NCAR Community Computing). Available at: https://doi.org/10.5065/qx9a-pg09.

D'ALEMBERT, J.R. 1752 Essai d'une Nouvelle Théorie de la Résistance des Fluides. *Tech. Rep.* de l'Academie Royale des Sciences de Paris, Paris, France. Available at: https://www.hachettebnf.fr/livre/essai-dune-nouvelle-theorie-de-la-resistance-des-fluides-9782329871394/.

DUPONT, S. & BRUNET, Y. 2008 Influence of foliar density profile on canopy flow: a large-eddy simulation study. *Agric. Forest Meteorol.* **148** (6-7), 976–990.

FINNIGAN, J., AYOTTE, K., HARMAN, I., KATUL, G., OLDROYD, H., PATTON, E., POGGI, D., ROSS, A. & TAYLOR, P. 2020 Boundary-layer flow over complex topography. *Boundary-Layer Meteorol.* **177**, 247–313.

FINNIGAN, J.J. 1983 A streamline coordinate system for distorted two-dimensional shear flows. *J. Fluid Mech.* **130**, 241–258.

FINNIGAN, J.J. 2000 Turbulence in plant canopies. *Annu. Rev. Fluid Mech.* **32** (1), 519–571.

FINNIGAN, J.J. 2004 A re-evaluation of long-term flux measurement techniques. Part II: coordinate systems. *Boundary-Layer Meteorol.* **113** (1), 1–41.

FINNIGAN, J.J. 2024 Streamline coordinates in three-dimensional turbulent flows. *J. Fluid Mech.* **999**, A101.

FINNIGAN, J.J. & BELCHER, S.E. 2004 Flow over a hill covered with a plant canopy. *Q. J. R. Meteorol. Soc.* **130**, 1–29.

FINNIGAN, J.J. & BRUNET, Y. 1995 Turbulent airflow in forests on flat and hilly terrain. In *Wind and Trees* (ed. M.P. COUTTS & J. GRACE), pp. 3–40. Cambridge University Press.

FINNIGAN, J.J., CLEMENT, R., MALHI, Y., LEUNING, R. & CLEUGH, H.A. 2003 A re-evaluation of long-term flux measurement techniques. Part I: averaging and coordinate rotation. *Boundary-Layer Meteorol.* **107**, 1–48.

FINNIGAN, J.J., RAUPACH, M.R., BRADLEY, E.F. & ALDIS, G.K. 1990 A wind tunnel study of turbulent flow over a two-dimensional ridge. *Boundary-Layer Meteorol.* **50** (1), 277–317.

FINNIGAN, J.J. & SHAW, R.H. 2008 Double-averaging methodology and its application to turbulent flow in and above vegetation canopies. *Acta Geophys.* **56** (3), 534–561.

FINNIGAN, J.J., SHAW, R.H. & PATTON, E.G. 2009 Turbulence structure above a vegetation canopy. *J. Fluid Mech.* **637**, 387–424.

GARRATT, J.R. 1992 *The Atmospheric Boundary Layer*. Cambridge University Press.

GONG, W. & IBBETSON, A. 1989 A wind tunnel study of turbulent flow over model hills. *Boundary-Layer Meteorol.* **49** (1-2), 113–148.

GRANT, E.R., ROSS, A.N., GARDINER, B.A. & MOBBS, S.D. 2015 Field observations of canopy flows over complex terrain. *Boundary-Layer Meteorol.* **156** (2), 231–251.

GRUBIŠIĆ, V. *et al.* 2008 The terrain-induced rotor EXperiment: a field campaign overview including observational highlights. *Bull. Am. Meteorol. Soc.* **89** (10), 1513–1534.

HARMAN, I.N., BÖHM, M., FINNIGAN, J.J. & HUGHES, D. 2016 Spatial variability of the flow and turbulence within a model canopy. *Boundary-Layer Meteorol.* **160** (3), 375–396.

HARMAN, I.N. & FINNIGAN, J.J. 2007 A simple unified theory for flow in the canopy and roughness sublayer. *Boundary-Layer Meteorol.* **123**, 339–363.

HARMAN, I.N. & FINNIGAN, J.J. 2008 Scalar concentration profiles in the canopy and roughness sublayer. *Boundary-Layer Meteorol.* **129** (3), 323–351.

HARMAN, I.N. & FINNIGAN, J.J. 2009 Flow over hills covered by a plant canopy: extension to generalised two-dimensional topography. *Boundary-Layer Meteorol.* **135** (1), 51–65.

HARMAN, I.N. & FINNIGAN, J.J. 2013 Flow over a narrow ridge covered with a plant canopy: a comparison between wind-tunnel observations and linear theory. *Boundary-Layer Meteorol.* **147** (1), 1–20.

HARMAN, I.N. & FINNIGAN, J.J. 2018 The SCION conifer wilding wind tunnel experiments: overview and first look at the data. *Tech. Rep*. EP189744. CSIRO, Canberra, Australia.

HARMAN, I.N. & FINNIGAN, J.J. 2021 Dispersal of seeds over complex terrain. In *Final Report on the Scion Conifer Wilding Project*. CSIRO.

HOUZE, R.A. *et al.* 2017 The olympic mountains experiment (OLYMPEX). *Bull. Am. Meteorol. Soc.* **98** (10), 2167–2188.

HUNT, J.C.R., LEIBOVICH, S. & RICHARDS, K.J. 1988 Turbulent shear flows over low hills. *Q. J. R. Meteorol. Soc.* **114**, 1435–1471.

HUNT, J.C.R. & SNYDER, W.H. 1980 Experiments on stably and neutrally stratified flow over a model three-dimensional hill. *J. Fluid Mech.* **96** (04), 671.

INOUE, M., MATHEOU, G. & TEIXEIRA, J. 2014 LES of a spatially developing atmospheric boundary layer: application of a fringe method for the stratocumulus to shallow cumulus cloud transition. *Mon. Weath. Rev.* **142** (9), 3418–3424.

ISHIHARA, T., HIBI, K. & OIKAWA, S. 1999 A wind tunnel study of turbulent flow over a three-dimensional steep hill. *J. Wind Engng Ind. Aerodyn.* **83** (1–3), 95–107.

JACKSON, P.S. & HUNT, J.C.R. 1975 Turbulent wind flow over a low hill. *Q. J. R. Meteorol. Soc.* **101**, 929–955.

KAIMAL, J.C. & FINNIGAN, J.J. 1994 *Atmospheric Boundary Layer Flows: Their Structure and Measurement*. Oxford University Press.

KATUL, G.G. & CHANG, W. 1999 Principal length scales in second-order closure models for canopy turbulence. *J. Appl. Meteorol.* **38** (11), 1631–1643.

KÖRNER, C. *et al.* 2005 Mountain systems. In *Ecosystems and Human Well-Being: Current State and Trends* (ed. R. HASSAN, R. SCHOLES & N. ASH), Millennium Ecosystem Assessment, vol. 1. Island Press.

LAGRULA, J. 1968 Hypsographic curve. In *Geomorphology*, pp. 542–544. Kluwer Academic Publishers.

LIU, Z., CAO, S., LIU, H. & ISHIHARA, T. 2019*a* Large-eddy simulations of the flow over an isolated three-dimensional hill. *Boundary-Layer Meteorol.* **170** (3), 415–441.

LIU, Z., DIAO, Z. & ISHIHARA, T. 2019*b* Study of the flow fields over simplified topographies with different roughness conditions using large eddy simulations. *Renew. Energy* **136**, 968–992.

LIU, Z., WANG, W., WANG, Y. & ISHIHARA, T. 2020 Large eddy simulations of slope effects on flow fields over isolated hills and ridges. *J. Wind Engng Ind. Aerodyn.* **201**, 104178.

LUMLEY, J.L. & PANOFSKY, H.A. 1964 *The Structure of Atmospheric Turbulence*. Interscience Publishers.

MA, Y., LIU, H., BANERJEE, T., KATUL, G.G., YI, C. & PARDYJAK, E.R. 2020 The effects of canopy morphology on flow over a two-dimensional isolated ridge. *J. Geophys. Res. Atmos.* **125** (19), e2020JD033027.

MASON, P.J. & KING, J.C. 1985 Measurements and predictions of flow and turbulence over an isolated hill of moderate slope. *Q. J. R. Meteorol. Soc.* **111**, 617–640.

MASON, P.J. & SYKES, R.I. 1979 Separation effects in Ekman layer flow over ridges. *Q. J. R. Meteorol. Soc.* **105**, 129–146.

MOENG, C.-H. & SULLIVAN, P.P. 2015 *Large-Eddy Simulation*, 2nd edn. Elsevier Ltd.

MUNTERS, W., MENEVEAU, C. & MEYERS, J. 2016 Turbulent inflow precursor method with time-varying direction for large-eddy simulations and applications to wind farms. *Boundary-Layer Meteorol.* **159** (2), 305–328.

NEFF, D.E. & MERONEY, R.N. 1998 Wind-tunnel modeling of hill and vegetation influence on wind power availability. *J. Wind Engng Ind. Aerodyn.* **74–76**, 335–343.

PATTON, E.G. & KATUL, G.G. 2009 Turbulent pressure and velocity perturbations induced by gentle hills covered with sparse and dense canopies. *Boundary-Layer Meteorol.* **133** (2), 189–217.

PATTON, E.G., SULLIVAN, P.P., SHAW, R.H., FINNIGAN, J.J. & WEIL, J.C. 2016 Atmospheric stability influences on coupled boundary layer and canopy turbulence. *J. Atmos. Sci.* **73**, 1621–1647.

POGGI, D. & KATUL, G.G. 2007*a* An experimental investigation of the mean momentum budget inside dense canopies on narrow gentle hilly terrain. *Agric. Forest Meteorol.* **144** (1–2), 1–13.

POGGI, D. & KATUL, G.G. 2007*b* Turbulent flows on forested hilly terrain: the recirculation region. *Q. J. R. Meteorol. Soc.* **133**, 1027–1039.

POGGI, D., KATUL, G.G., ALBERTSON, J.D. & RIDOLFI, L. 2007 An experimental investigation of turbulent flows over a hilly surface. *Phys. Fluids* **19** (3), 036601.

POGGI, D., KATUL, G.G., FINNIGAN, J.J. & BELCHER, S.E. 2008 Analytical models for the mean flow inside dense canopies on gentle hilly terrain. *Q. J. R. Meteorol. Soc.* **1112**, 1095–1112.

POGGI, D., PORPORATO, A., RIDOLFI, L., ALBERTSON, J.D. & KATUL, G.G. 2004 The effect of vegetation density on canopy sub-layer turbulence. *Boundary-Layer Meteorol.* **111** (3), 565–587.

PRANDTL, L. 1904 Motion of fluids with very little viscosity. In *Technical Memorandum*, vol. 452. National Advisory Committee for Aeronautics.

RAUPACH, M.R. 1994 Simplified expressions for vegetation roughness length and zero-plane displacement height. *Boundary-Layer Meteorol.* **71**, 211–216.

RAUPACH, M.R., FINNIGAN, J.J. & BRUNET, Y. 1996 Coherent eddies and turbulence in vegetation canopies: the mixing-layer analogy. *Boundary-Layer Meteorol.* **78** (3), 351–382.

ROSS, A.N. 2008 Large-eddy simulations of flow over forested ridges. *Boundary-Layer Meteorol.* **128** (1), 59–76.

ROSS, A.N. & VOSPER, S.B. 2005 Neutral turbulent flow over forested hills. *Q. J. R. Meteorol. Soc.* **131**, 1841–1862.

SCHLATTER, P., ADAMS, N.A. & KLEISER, L. 2005 A windowing method for periodic inflow/outflow boundary treatment of non-periodic flows. *J. Comput. Phys.* **206** (2), 505–535.

SHAW, R.H. & PATTON, E.G. 2003 Canopy element influences on resolved- and subgrid-scale energy within a large-eddy simulation. *Agric. Forest Meteorol.* **115**, 5–17.

SULLIVAN, P.P., MCWILLIAMS, J.C. & PATTON, E.G. 2014 Large-eddy simulation of marine atmospheric boundary layers above a spectrum of moving waves. *J. Atmos. Sci.* **71** (11), 4001–4027.

SULLIVAN, P.P., MCWILLIAMS, J.C., WEIL, J.C., PATTON, E.G. & FERNANDO, H.J.S. 2020 Marine boundary layers above heterogeneous SST: across-front winds. *J. Atmos. Sci.* **77** (12), 4251–4275.

SULLIVAN, P.P., MCWILLIAMS, J.C., WEIL, J.C., PATTON, E.G. & FERNANDO, H.J.S. 2021 Marine boundary layers above heterogeneous SST: along-front winds. *J. Atmos. Sci.* **78**, 3297–3315.

SULLIVAN, P.P. & PATTON, E.G. 2011 The effect of mesh resolution on convective boundary layer statistics and structures generated by large-eddy simulation. *J. Atmos. Sci.* **68** (10), 2395–2415.

TAMURA, T., OKUNO, A. & SUGIO, Y. 2007 LES analysis of turbulent boundary layer over 3D steep hill covered with vegetation. *J. Wind Engng Ind. Aerodyn.* **95** (9-11), 1463–1475.

TAYLOR, P.A., MASON, P.J. & BRADLEY, E.F. 1987 Boundary-layer flow over low hills. *Boundary-Layer Meteorol.* **39** (1–2), 107–132.

TOLLADAY, J. & CHEMEL, C. 2021 Numerical modelling of neutral boundary-layer flow across a forested ridge. *Boundary-Layer Meteorol.* **180** (3), 457–476.

WILCZAK, J.M., ONCLEY, S.P. & STAGE, S.A. 2001 Sonic anemometer tilt correction algorithms. *Boundary-Layer Meteorol.* **99**, 127–150.

WILSON, J.D., FINNIGAN, J.J. & RAUPACH, M.R. 1998 A first-order closure for disturbed plant-canopy flows, and its application to winds in a canopy on a ridge. *Q. J. R. Meteorol. Soc.* **124** (547), 705–732.

WOOD, N. 2000 Wind flow over complex terrain: a historical perspective and the prospect for large-eddy modelling. *Boundary-Layer Meteorol.* **96**, 11–32.

WOOD, N. & MASON, P. 1993 The pressure force induced by neutral, turbulent flow over hills. *Q. J. R. Meteorol. Soc.* **119** (514), 1233–1267.

YOUNG, G.S. & PIELKE, R.A. 1983 Application of terrain height variance spectra to mesoscale modeling. *J. Atmos. Sci.* **40** (10), 2555–2560.